Journal of Sol-Gel Science and Technology (2025) 115:1694–1714
https://doi.org/10.1007/s10971-025-06882-7

ORIGINAL PAPER

Role of Mg substitution in modulating defect-mediated magnetism and mechanical strength of $Zn_{0.95}Co_{0.05}O$ systems

E. Asikuzun[1] · G. Yildirim[2] · A. S. Ertürk[3] · O. Ozturk[4] · T. Seydioglu[5] · C. Terzioglu[6,7]

Received: 16 June 2025 / Accepted: 13 July 2025 / Published online: 31 July 2025

Abstract

This study investigates the structural, magnetic, and mechanical modifications induced by partial Mg/Zn substitution in $Zn_{0.95}Co_{0.05}O$ diluted magnetic semiconductor (DMS) systems prepared by the sol-gel method. A combination of X-ray diffraction (XRD), scanning electron microscopy (SEM), vibrating sample magnetometry (VSM), and Vickers microhardness (H_v) testing is employed to assess the impact of Mg incorporation. Experimental and computational results confirm the successful substitution of Mg^{2+} ions into the ZnCoO lattice without forming secondary phases. XRD analyses reveal a slight reduction in crystallite size, varying from 37.62 nm to 36.48 nm, attributable to the differences in ionic radius and electronegativity between Mg^{2+} and Zn^{2+} ions. Mg addition enhances crystallinity, interface state formation, and atomic-scale interactions, while promoting quantum confinement effects. SEM observations indicate that Mg/Zn substitution significantly influences particle size, surface morphology, and oxide layer thickness. Increasing Mg content improves grain coupling and surface uniformity through strengthened interfacial interactions. Microhardness results show that Mg incorporation improves mechanical stability by limiting crack propagation, enhancing grain boundary couplings, and minimizing stored internal strain energy. Magnetic measurements indicate that all samples exhibit predominantly paramagnetic behavior with weak ferromagnetic features emerging at low temperatures. Low-temperature magnetization is attributed to defect-mediated ferromagnetic coupling, whereas high-temperature behavior follows Curie–Weiss paramagnetism. The Mg/Zn substitution alters electronic structure and oxygen vacancy distribution, modulating exchange interactions. Small coercivity values (230 Oe in ZFC and 570 Oe in FC) and vertical M–H loop shifts at 5 K suggest diluted antiferromagnetism rather than conventional exchange bias effects. Additionally, creep analysis from loading–unloading curves confirms that increasing Mg content lowers the creep rate, with the ZnO: Mg (5%) sample exhibiting the best mechanical resilience. In conclusion, Mg substitution significantly enhances the structural, magnetic, and mechanical performance of ZnCoO matrices, making them more favorable for controlled paramagnetic applications than room-temperature spintronic technologies.

✉ G. Yildirim
yildirim_g@ibu.edu.tr

[1] Department of Metallurgical and Materials Engineering, Kastamonu University, Kastamonu, Turkey

[2] Department of Mechanical Engineering, Bolu Abant Izzet Baysal University, Bolu, Turkey

[3] Department of Basıc Pharmaceutıcal Sciences, Adiyaman University, Adiyaman, Turkey

[4] Department of Electrical and Electronics Engineering, Kastamonu University, Kastamonu, Turkey

[5] Department of Electronics and Automation, Kastamonu University, Kastamonu, Turkey

[6] Department of Physics, Bolu Abant Izzet Baysal University, Bolu, Turkey

[7] Center of Nuclear Radiation Detectors Research and Applications, BAIBU, Bolu, Turkey

Graphical Abstract

Fundamental Structural Properties of $Zn_{0.95-x}Mg_xCo_{0.05}O$ DMS structure.

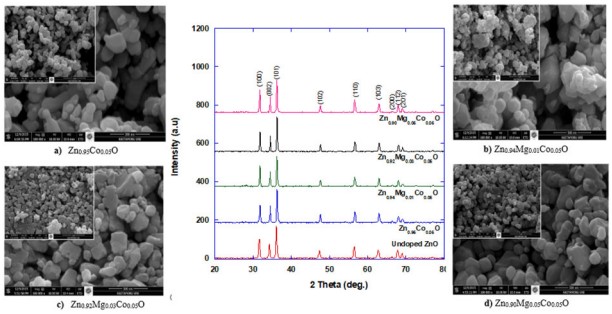

Keywords Diluted magnetic semiconductor · Mg/Zn substitution · Coupling strength · Paramagnetism

Highlights

- Production of advanced ceramic materials with desired superior properties using the Sol-Gel method.
- Influence of Mg/Zn substitution on electronic structure, oxygen vacancies, and defect-mediated exchange interactions.
- Improvement in crystalline quality and surface morphology view with Mg impurity.
- Change of non-recoverable stress amplified areas and stored internal strain energy with Mg impurity.
- Development of grain couplings and quantum confinement effects based on replacement mechanism.

1 Introduction

Diluted Magnetic Semiconductors (DMS), a distinct class of semiconductor materials, consist of a non-magnetic semiconductor doped with a small percentage of magnetic ions, where a fraction of the host semiconductor atoms is substituted or doped with a magnetic transition metal or rare-earth metal ions [1]. The doping process introduces magnetic properties while preserving the intrinsic semiconductor characteristics, enabling unique functionalities for advanced applications. The magnetism in DMS primarily arises from the interaction between the localized magnetic moments of doped ions and charge carriers within the semiconductor. The exchange interaction between doped ions and charge carriers results in various magnetic phenomena, such as room-temperature ferromagnetism, which is crucial for practical applications. Additionally, external stimuli to DMS materials, viz, temperature, pressure, or electric fields, play a significant role in tuning the electronic band structure and magnetic behavior, further enhancing their real-world applicability. In this respect, DMS materials have garnered significant interest due to their ability to combine both semiconducting and magnetic properties within a single material system.

Moreover, DMS materials have attracted considerable attention as emerging candidates for the engineering and microelectronics industry owing to their unique spin-dependent magneto-electro-optical properties, resulting from the coupling between semiconductor bands and localized states [2]. Similarly, the valuable feature makes the DMS foundational materials for the fields of spintronics (exploiting both the electron charge and its intrinsic spin to develop next-generation electronic devices) and magneto-optoelectronics, enabling the development of a wide range of semiconductor devices such as spin-polarized light-emitting diodes, spin-based lasers, and spin-transistor logic devices. In this context, DMS materials provide an innovative platform where physical properties (especially bandgap energy and magnetism) are not only dependent on particle size but also on doping concentration [3]. The advancement of these devices is considered a potential route for extending the semiconductor scaling roadmap toward spin-enhanced electronics [2, 4].

In conclusion, DMS materials with superior features are regarded as promising candidates for advanced applications in quantum computing, spintronics, and magneto-optical devices. In particular, ZnO-based DMS materials have attracted significant interest in recent years because of their potential applications in various technological fields, including thermal glass, piezoelectric devices, solar cells, solid-state gas sensors, surface acoustic wave devices, laser systems, microelectromechanical systems, organic light-emitting diodes, and spintronic devices (read heads in magnetic hard disks and giant magnetoresistance systems). Spintronic technology seems to be a viable alternative to conventional semiconductor-based memory production, offering improved performance and energy efficiency. As a result, research efforts in both fundamental science and

advanced technological development increase steadily, driving further advancements in the field [5–10].

Moreover, ZnO structure has been known to play a crucial role in advancing television technology by significantly enhancing the magnetic properties of nickel-iron alloys [11]. Snoek (1946) demonstrated that substituting NiO with ZnO in specific proportions improved the magnetic properties of ferrite-based materials [12]. For example, it was found that when ZnO is incorporated at a molar weight percentage of 35%, the magnetic permeability of ferrite increases by 3000% [13]. This effect occurs as Zn^{2+} ions introduced into the crystal structure displace Fe^{3+} ions from tetrahedral positions, leading to augmented magnetic performance. The significant enhancement in magnetic properties is primarily attributed to octahedral units containing a higher concentration of magnetic atoms compared to tetrahedral units. In addition to enhancing magnetic characteristics, the incorporation of the ZnO compound also lowers the Curie temperature of the structure and thus reduces electrical losses.

Recent studies have revealed that ZnO is not only an effective doping material but can also exhibit intrinsic ferromagnetic properties when combined with specific elements. In particular, the incorporation of Mn, Co, and Fe atoms into the ZnO structure has been shown to induce ferromagnetism in ZnO nanostructure applications [14–20].

However, several fundamental challenges, such as an intrinsically low Curie temperature, significant structural defects, and high sensitivity to environmental factors (moisture and oxygen), hinder the practical application of ZnO-based DMS materials. Additionally, variations in production parameters, including precursor concentration, reaction temperature, and annealing conditions, contribute to inhomogeneous doping levels and the non-uniform distribution of magnetic dopants along the crystal structure. The weak magnetic response at room temperature and undesirable interactions between dopant ions and charge carriers further compromise the conductivity and magnetic performance of ZnO-based DMS nanostructures. In particular, the inconsistency in magnetic behavior stems from the uneven distribution of additives, the presence of structural defects, and variations in synthesis conditions, making it difficult to achieve stable, high-performance, and reproducible magnetic properties. As a result, the magnetic performance of ZnO-based DMS may not be sufficient to meet the stringent requirements for real-world applications.

Nonetheless, precise control over synthesis parameters, optimized doping strategies, and advancements in material engineering can significantly enhance the balance between conductivity and magnetism through the materials. All the improvements are crucial for unlocking the full potential of ZnO-based DMS in various technological applications, including spintronics and magneto-optoelectronic devices.

This study aims to determine the change in the structural, magnetic, and micromechanical features of Mg/Zn partially substituted $Zn_{0.95-x}Mg_xCo_{0.05}O$ diluted magnetic nano-bulk semiconductor materials concerning X-ray diffraction (XRD), scanning electron microscopy (SEM), vibrating sample magnetometry (VSM), and Vickers microhardness (H_v) measurements. The effect of extra alkaline earth metal in the ZnO-based DMS material on the fundamental features is sensitively discussed. Establishing the relationships will facilitate the development of an optimum Mg/Zn-replaced ZnO-based DMS compound with customized functionalities tailored for specific areas. Moreover, this study will offer comprehensive insights into the potential technological applications of the synthesized materials. For instance, microhardness measurements indicate that Mg-doped ZnO is a promising candidate for piezoelectric devices due to its enhanced mechanical properties. Additionally, ZnO-based semiconductor thin films are widely utilized in several application fields, including thermal glass, piezoelectric devices, solar cells, solid-state gas sensors, surface acoustic wave devices, laser systems, MEMS, and OLEDs.

All in all, the motivation behind the comprehensive study stems from the urgent need to develop mechanically robust and functionally versatile DMS ceramic materials for next-generation electronic, magnetic, and structural applications. While ZnO-based DMS systems (especially Co-doped ZnO) offer promising features such as a wide bandgap and tunable magnetic behavior for spintronic technologies, their practical implementation is hindered by some inherent problems, including mechanical fragility, phase instability, and inconsistent magnetic responses. This research hypothesizes that partial substitution of Zn with Mg in $Zn_{0.95}Co_{0.05}O$ semiconducting ceramics can effectively stabilize the wurtzite crystal structure, enhance mechanical integrity through mechanisms such as grain boundary reinforcement and dislocation pinning, and fine-tune magnetic interactions via defect engineering. Hence, this work bridges a critical gap between magnetic functionality and mechanical durability in $Zn_{0.95-x}Mg_xCo_{0.05}O$ DMS materials. By systematically investigating the influence of Mg incorporation on the structural, magnetic, and mechanical characteristics of bulk ZnCoO ceramics, the study aims to establish a clear structure–property relationship and pave the way for DMS materials optimized for real-world applications such as magneto-mechanical sensors, MEMS/NEMS devices, and magnetic memory components.

2 Experimental procedure

The bulk $Zn_{0.95-x}Mg_xCo_{0.05}O$ DMS structure system is synthesized using the sol-gel method with varying Mg

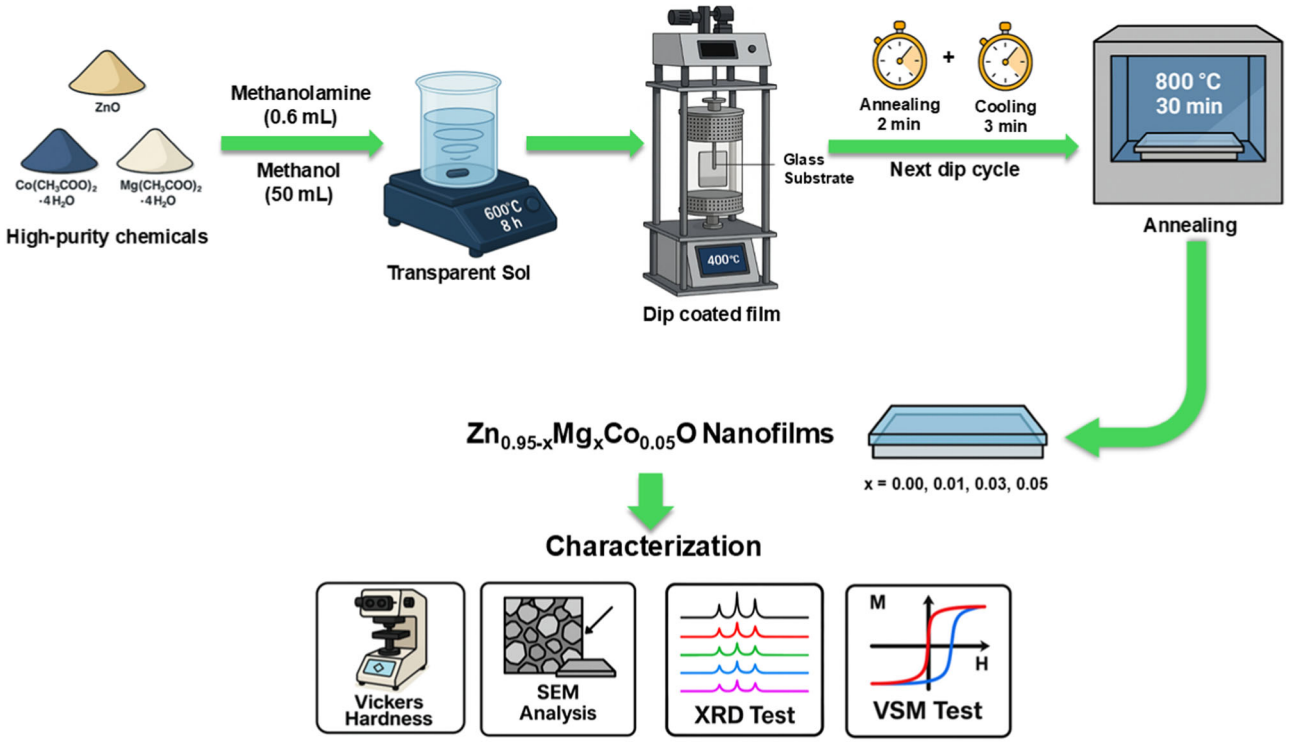

Fig. 1 Representative scheme for $Zn_{0.95-x}Mg_xCo_{0.05}O$ nanoparticles: fabrication to fundamental characteristic properties

substitution concentrations ($x = 0.00$, 0.01, 0.03, and 0.05). Our main motivation for using the sol-gel method is that physical and chemical preparation methodologies are extensively employed in the production of complex nanostructures, including semiconductors, perovskite manganites, and superconductors across multiple scales [21, 22]. In this respect, the use of the sol-gel method is especially significant, as the technique enables precise compositional control, homogeneity at the molecular level, and low-temperature synthesis, such as critical factors in tailoring nanoscale features, defect distribution, and interface quality in complex oxide systems. This synthesis approach directly influences the observed property enhancements by facilitating fine microstructural tuning and dopant incorporation [23]. A detailed representative scheme based on the production stage is given in Fig. 1 in detail. A variety of techniques have been developed for the deposition of semiconducting ZnO nanostructures (nanorods, nanowires, and nanoparticles) as regards radio-frequency magnetron sputtering, pulsed laser deposition, spin coating, chemical vapor deposition, spray pyrolysis, atomic layer deposition, and solution-based deposition methods [24]. Among the production methods, the sol-gel (SG) process has emerged as a widely utilized solution-based deposition technique due to its numerous advantages based on its effectiveness and versatility [25, 26]. This method facilitates low-temperature synthesis compared to techniques regarding pulsed laser and chemical vapor deposition, making SG particularly effective for the controlled growth of semiconducting ZnO nanostructures. Similarly, in contrast to vacuum-based deposition techniques such as radio-frequency magnetron sputtering and PLD, the SG method is both cost-effective and easily scalable, as it does not require expensive equipment or high-vacuum conditions. Moreover, one of the primary advantages of the SG technique is its ability to produce highly pure and homogeneous materials with well-controlled stoichiometry and well-defined particle size distributions. Besides, the method provides excellent control over the chemical composition, microstructure, crystallinity, and morphology of ZnO materials by adjusting synthesis parameters such as precursor concentration, dopant purity, reaction temperature, and aging time. Thus, the ZnO nanostructures present a high surface-area-to-volume ratio. Moreover, the SG process allows for the incorporation of dopants and the engineering of defect structures, enabling the modification of electronic band structure and magnetic features belonging to ZnO structures. This flexibility is crucial for designing transparent conductive oxides, photocatalytic materials, and ZnO-based diluted magnetic semiconductors (DMSs). As a result, compared to vacuum-based and high-temperature methods, the SG process is considered environmentally friendly, as the method involves relatively mild reaction conditions and generates fewer hazardous byproducts. Additionally, the SG

fabrication method also provides precise control over the chemical composition of the final material, allowing the fine-tuning of optical, electrical, magnetic, and catalytic properties to meet specific application requirements. In summary, the sol-gel method is perfect for the production of ZnO diluted magnetic semiconductors in every respect.

In this study, high-purity precursors, including zinc oxide (98.0–101.0% purity), cobalt acetate tetrahydrate (99.9% purity), and magnesium acetate tetrahydrate (99.9% purity), are utilized for solution preparation. Methanolamine (0.6 mL) and methanol (50 mL) are added as solvents, and the solution is continuously stirred with a magnetic stirrer at a constant temperature value of 60 °C for the duration of 8 h to ensure homogeneity. For this stage, the most critical aspect is maintaining a transparent solution with no precipitation or granulation.

Glass substrates are coated in a vertical furnace at 400 °C using the dip-coating method. After each dip, the coated nano-thin films underwent an annealing process at the same temperature for 2 min, followed by a cooling period of 3 min before subsequent dipping. The final heat treatment is performed at 800 °C for 30 min to enhance the structural and functional properties of the films. The resulting nano-thin film samples were designated as $Zn_{0.90}Mg_{0.05}Co_{0.05}O$, $Zn_{0.92}Mg_{0.03}Co_{0.05}O$, $Zn_{0.94}Mg_{0.01}Co_{0.05}O$, and $Zn_{0.95}Co_{0.05}O$.

At the same time, we can summarize the basic motivations for considering homovalent Mg and Zn substitution in the lattice as follows.

- Mg^{2+} ion, due to its similar valence, electronegativity, and bonding behavior, is a suitable homovalent substitute for Zn^{2+} in the $Zn_{0.95-x}Mg_xCo_{0.05}O$ lattice, enabling energetic favorability and structural integration without compromising the crystal integrity. Accordingly, the presence of optimum Mg significantly enhances the structural, optical, and electronic properties of ZnO by modifying its crystal lattice, defect chemistry, and charge carrier dynamics.
- Secondly, magnesium is selected as the dopant in this study due to its unique combination of structural compatibility, chemical stability, and non-magnetic nature, which collectively support the goals of optimizing mechanical performance and tuning magnetic behavior in $Zn_{0.95-x}Mg_xCo_{0.05}O$ DMS structures due to the similar features. In particular, the ionic radius of Mg^{2+} (0.72 Å) closely matches that of Zn^{2+} (0.74 Å), allowing seamless substitution within the wurtzite ZnO lattice without introducing significant lattice distortions or unwanted secondary phases. Thus, the existence of optimum Mg ions in the system promotes better crystallinity, reduces grain size, and strengthens intergranular bonding. Unlike other transition metal dopants that can introduce complex or unpredictable magnetic interactions, Mg is non-magnetic, making it ideal for investigating subtle, defect-mediated magnetic phenomena in the presence of Co^{2+} ions without overlapping magnetic contributions.
- Mg is known to enhance mechanical properties by acting as an artificial barrier to dislocation motion, strengthening grain boundaries, and minimizing internal strain energy; these are critical properties for improving the structural integrity of ceramic matrices. Its incorporation also influences charge distribution and defect chemistry, such as oxygen vacancy concentration, which plays a key role in controlling magnetic and electronic responses.
- Mg is chemically stable, non-toxic, and environmentally benign, making it a safe and sustainable choice for functional ceramic applications. Altogether, using Mg as a dopant enables a scientifically controlled and multifaceted approach to improving both the mechanical and magnetic performance of ZnCoO-based bulk DMS materials, distinguishing this study from conventional doping strategies that primarily focus on magnetic enhancement.
- As for optical properties, Mg incorporation can widen the bandgap of ZnO due to the higher electronegativity and energy level of Mg compared to Zn ions, making Mg-doped ZnO suitable for UV optoelectronic applications such as UV detectors and transparent conducting oxides. Additionally, Mg alters the concentration and distribution of intrinsic defects such as oxygen vacancies and zinc interstitials, which play a key role in tailoring photoluminescence properties and modulating carrier recombination rates.
- Electronically, Mg doping can also improve charge carrier mobility and control n-type conductivity by influencing defect levels and suppressing unwanted deep-level states. All in all, Mg acts as a versatile dopant that not only preserves the desirable features of ZnO but also enhances its functional performance across structural, optical, and electronic domains.

2.1 Characterization studies

2.1.1 H_v experiments

Micro-indentation hardness experiments are conducted on Mg/Zn partially substituted $Zn_{0.95-x}Mg_xCo_{0.05}O$ diluted magnetic structures using a UMT-Bruker, SYS2 digital microhardness tester to investigate the effect of substitution mechanism in the ZnO-based DMS nanostructures. The tests are performed under applied loads ranging from 0.5 N to 2.0 N, with indentations performed at five different locations for 10 s. A Vickers-type diamond indenter with a

two μm tip diameter is utilized in the system. In the instrumented indentation technique, all relevant parameters, including indenter depth and applied load, are continuously recorded during elastic and plastic deformation. This method eliminates the need for optical measurement of indentation diagonals. This methodology enables precise assessment of material hardness, which is critical for understanding mechanical properties such as deformation resistance and toughness. Investigating the microhardness of $Zn_{0.95-x}Mg_xCo_{0.05}O$ DMS structure is essential to evaluating the impact of Mg/Zn partial substitution on mechanical performance. Vickers hardness test results provide insights into key factors such as interactions between hexagonal layers, resistance to external forces, crack orientation/geometry, grain boundary problems, stored internal strain energy for crack propagation, active operable slip system mechanism (AOSSm), deformation and granularity degree (D/DG), surface residual compressive stress areas (SRCSa), artificial force barriers (AFB), intergranular interactions, non-recoverable stress amplified areas (n-RSAa) within the matrix.

2.1.2 SEM experiments

High-resolution field-emission SEM (Quanta FEG 250, FEI, USA) is employed to examine the microstructural features belonging to Mg/Zn partially substituted $Zn_{0.95-x}Mg_xCo_{0.05}O$ DMS structures at 5000× magnification using secondary electron imaging (SEI) mode with a 20 kV accelerating voltage. The SEM images assess the influence of Mg/Zn partial substitution on the surface uniformity, particle size distribution, smoothness, crystalline orientation, and crystallinity problems, such as microscopic structural defects, porosity, microcracks, voids, grain (mis) alignments, and grain boundary coupling. The observations establish a relationship between microstructural characteristics and other (magnetic and micromechanical) features, providing valuable insights into its stability, durability, and suitability for applications in technological, spintronics, magneto-optoelectronic devices, and high-performance electronic systems.

2.1.3 Powder XRD measurements

XRD analysis is employed primarily to complement the experimental findings obtained from SEM and H_v experimental measurements. XRD data are acquired using a Bruker D8 Advance powder X-ray diffractometer equipped with a CuK_α radiation source ($\lambda = 1.54$ Å), operating at 40 mA and 40 kV in an air environment at room temperature. The measurements are conducted over a 2θ range of 3°–90° with a scan rate of 2° per minute and a step size of 0.02°. The diffraction peaks are indexed using the JCPDS-ICDD reference card of 36-1451, corresponding to a hexagonal wurtzite crystal structure without evidence of any distortions. In the XRD patterns, the diffraction peaks are labeled as (*hkl*). The diffraction peaks obtained provide critical insights into structural characteristics, including crystalline quality, grain size, grain orientation distribution, texturing, and the coupling strength between hexagonal layers.

2.1.4 VSM measurements

Magnetic analysis is essential for advancing and optimizing diluted magnetic semiconductors. In this study, magnetization hysteresis curves are utilized to investigate the fundamental magnetic characteristics (magnetic ordering, coercivity, remanence, and saturation magnetization) of ZnO-based DMS nanostructures with Mg/Zn partial replacement mechanism. The curves to be recorded serve as key indicators of the diamagnetic behavior of ZnO-based DMS nanostructures, with the area under the hysteresis loop (dM/dH) commonly employed to evaluate their magnetic response. Magnetic characterization of the synthesized samples is performed using a Lake Shore 7407 vibrating sample magnetometer (VSM). The measurements are conducted at a temperature of 15 K under an applied magnetic field ranging from ±2 T. The *M–H* curves provide a comprehensive analysis of the response of ZnO-based DMS nanostructures to applied magnetic field strengths, enabling the evaluation of their magnetic behavior. On this basis, VSM analysis plays a crucial role in determining the optimal Mg/Zn concentration levels required for tailoring the magnetic properties to meet the specific requirements of spintronic applications.

3 Results and discussions

3.1 Fundamental magnetic characteristics of $Zn_{0.95-x}Mg_xCo_{0.05}O$ DMS nanostructures

3.1.1 Magnetization hysteresis curves for semiconducting materials

The *M–H* curves presented in Figs. 2 and 3 illustrate the magnetic behavior of Mg/Zn partially substituted $Zn_{0.95-x}Mg_xCo_{0.05}O$ diluted magnetic nano-bulk semiconductor materials at various environmental temperatures intervals 10 K–300 K. It was known that the magnetic features are primarily influenced by the interplay between Co doping, Mg substitution, intrinsic defects, and carrier-mediated exchange interactions through the semiconducting matrix. It is obvious from the figures that the *M–H* curves shed some light on the effects of the Mg/Zn partial replacement mechanism on the magnetic response of the ZnO-based DMS systems under applied magnetic field strengths. Figures 2 and 3 indicate that for

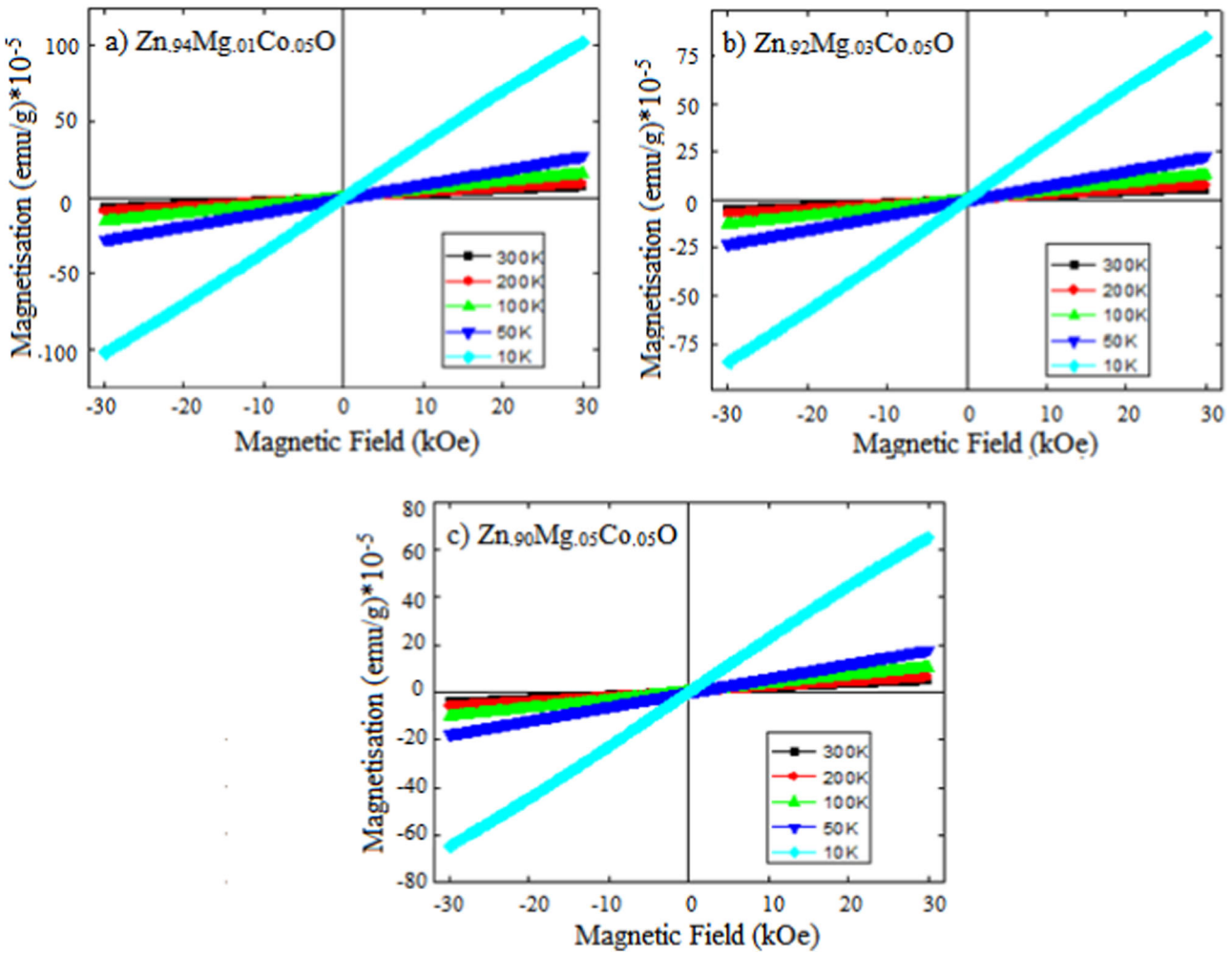

Fig. 2 Magnetic hysteresis loops of **a** Zn0.94Mg0.01Co0.05O; **b** Zn0.92Mg0.03Co0.05O; **c** Zn0.90Mg0.05Co0.05O at various temperatures

all the compounds studied, there appears to be a predominantly linear magnetic response at any temperature value, confirming that the dominant magnetic contribution is paramagnetic. The lack of remarkable hysteresis (presence of small hysteresis) reveals weak or negligible ferromagnetic ordering at the Mg/Zn substitution concentration levels. Besides, a slight increase in magnetization at lower temperatures hints at weak ferromagnetic coupling stemming from defect-mediated exchange interactions. According to figures, at lower temperature regions (up to 50 K), the magnetization values are slightly larger as compared to those at higher temperatures (between 200 K and 300 K). The main reason for the slight enhancement in the magnetization is due to the thermal activation of localized magnetic moments at lower temperature regions. In the case of higher temperature regions, the magnetization (vanishing coercivity) diminishes due to thermal fluctuations disrupting spin magnetic moment alignment, confirming the Curie–Weiss paramagnetic behavior. The general linear paramagnetic-like behavior of the curves at higher temperature regions indicates a dominant paramagnetic nature. In other words, the reduction of the alignments with thermal energy leads to the weakening of the overall magnetic response. Accordingly, due to the weak ferromagnetic behavior at low-temperature regions, the Mg/Zn substitution mechanism is not ideal for room-temperature spintronic applications without further optimization. At the same time, Figs. 2 and 3 reveal that the different substitution levels of Mg ions subtly influence the magnetic response. On this basis, the magnetization values increase slightly with increasing Mg concentration from $x = 0.01$ to $x = 0.05$. This is attributed to the fact that non-magnetic Mg incorporation may influence defect-mediated exchange interaction magnetism, likely by modifying carrier concentration, electron density, or structural defects, which indirectly affect the Co–Co magnetic interactions. Besides, it can be pointed out that the presence of Co ions in the semiconducting matrix may remain largely isolated paramagnetic centers with only limited interaction between the Co ions. The absence of a clear ferromagnetic loop suggests that Mg/Zn substitution does not induce strong long-range ferromagnetic ordering due to the non-magnetic behavior of Mg atoms. However, a higher Mg concentration may reduce

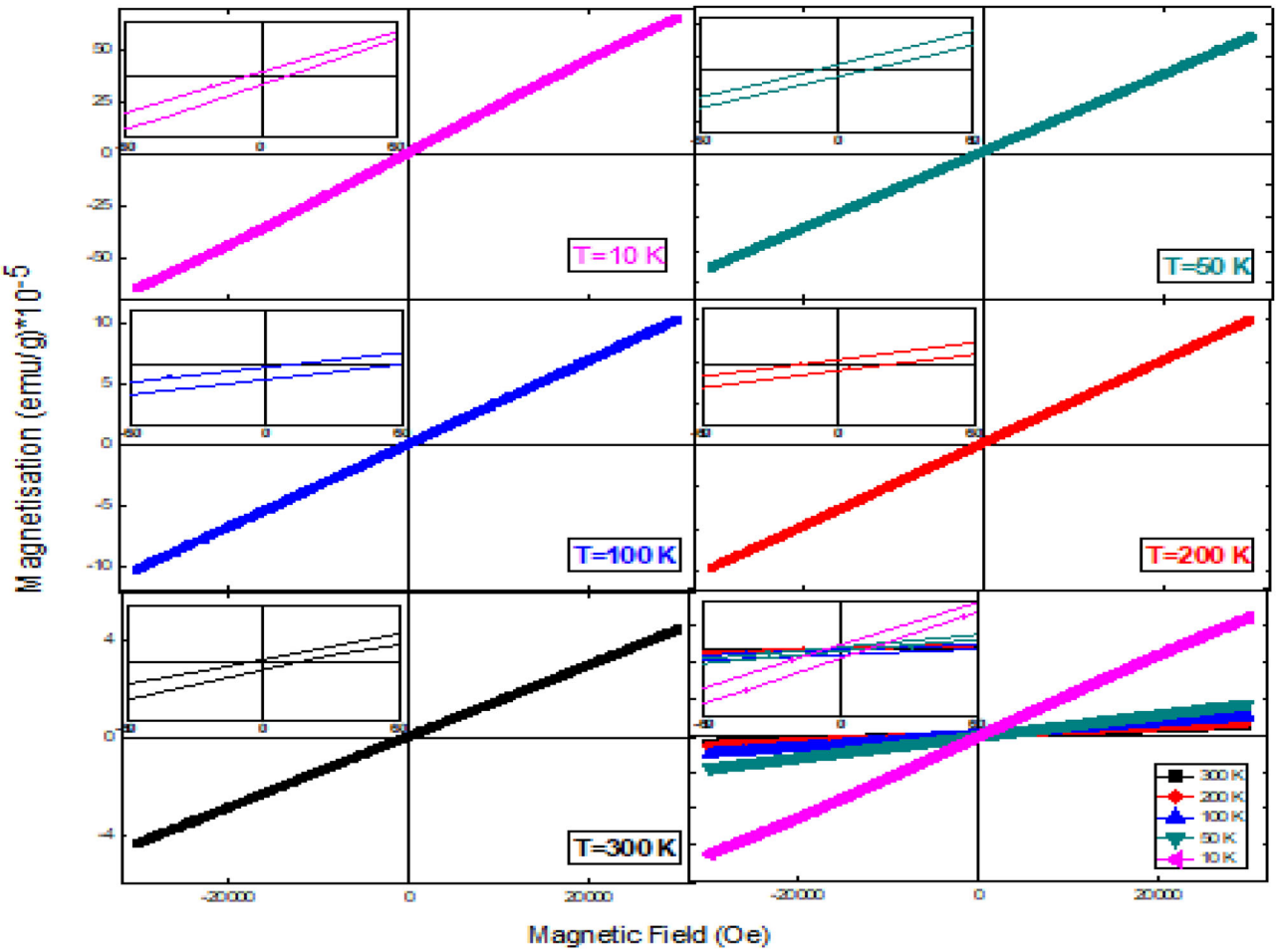

Fig. 3 *M–H* loops of $Zn_{0.90}Mg_{0.05}Co_{0.05}O$ 800 °C for 30 min are drawn at some selected temperatures. Innermost small graphics, which are built into the great graphics, show the zoomed part of *M–H* curves for corresponding temperature with a magnetic field scale of ±60 Oe

available charge carriers, thereby weakening potential carrier-mediated ferromagnetic interactions. Correspondingly, the substitution role is more related to altering the electronic structure, oxygen vacancies, and defect-mediated exchange interactions rather than directly contributing to magnetic characteristics. As for the field dependence of the newly synthesized matrix, the magnetization exhibits a nearly symmetric and reversible behavior concerning the external magnetic field strengths. The lack of coercivity and remanence (narrow hysteresis loops) in the *M–H* curves further indicates the conclusion that the dominant magnetic interactions in the ZnO lattice are weak long-range ferromagnetic ordering. Based on the results deduced from the figures, Mg/Zn partially replaced ZnO matrices seem to be more suitable for applications where controlled paramagnetic behavior is required rather than robust ferromagnetic ordering for spintronic applications.

Moreover, Fig. 4 sketches in detail the temperature-dependent magnetic susceptibility (χ) of $Zn_{0.95-x}Mg_xCo_{0.05}O$ DMS structures with varying Mg ion concentrations ($x = 0.00$, 0.01, 0.03, and 0.05). Every sample studied presents higher susceptibility values at lower temperatures. However, as the ambient temperature increases, the χ value decreases significantly. Notably, a pronounced reduction of susceptibility is observed up to 50 K. Beyond 200 K, the decrease becomes minimal, indicating a stabilization in susceptibility behavior. Furthermore, small variations in χ among various compositions reveal that non-magnetic Mg ion concentrations vary slightly in the density of magnetic interactions. At any temperature region, the $Zn_{0.94}Mg_{0.01}Co_{0.05}O$ semiconducting structure possesses the largest χ parameters as compared to those of $Zn_{0.92}Mg_{0.03}Co_{0.05}O$ and $Zn_{0.90}Mg_{0.05}Co_{0.05}O$ structures. At the same time, all semiconducting compounds exhibit a peak in susceptibility at lower temperatures, meaning the dominance of localized magnetic interactions. Besides, the considerable enhancements in χ values at lower temperature regions result from a typical Curie–Weiss-like paramagnetic feature that is the conventional behavior of DMS structures. Additionally, Fig. 4 shows the decline in χ parameters with increasing ambient temperature values due to the reduction in the alignment of magnetic moments, depending on the thermal agitation.

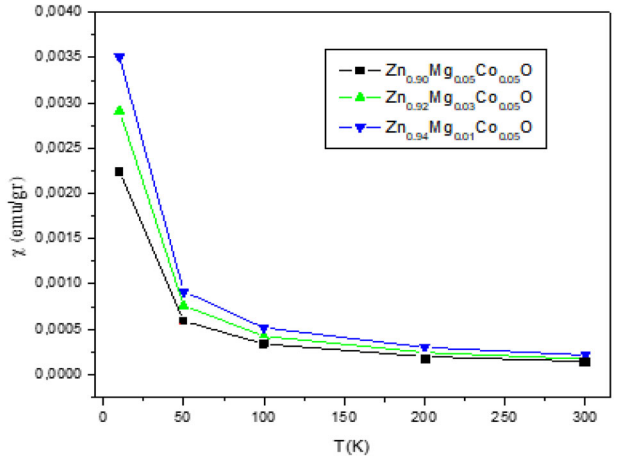

Fig. 4 Temperature dependence of the susceptibility of the samples

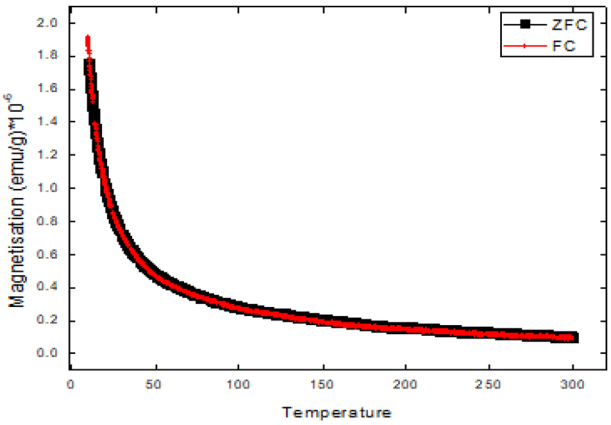

Fig. 5 Temperature variation of magnetization of $Zn_{0.90}Mg_{0.05}Co_{0.05}O$ at 800 °C for 30 min under 100 Oe applied magnetic field

Beyond the temperature of 200 K, the χ parameter remains nearly constant, reflecting a transition to a predominantly paramagnetic state, where thermal energy disrupts any short-range magnetic correlations.

In addition, the $Zn_{0.95-x}Mg_xCo_{0.05}O$ DMS structures with different Mg ion concentrations exhibit similar trends. However, the values of χ parameters change slightly, implying that non-magnetic Mg ions play an important role in modifying the defect structure and carrier concentration. As discussed above, the Mg ions do not contribute directly to magnetization but may vary Co^{2+} spin magnetic moment interactions by altering charge carrier density or modifying oxygen vacancies. On the other hand, a higher Mg ion concentration level slightly augments the susceptibility at low-temperature regions as a result of possible modifications in the exchange interactions between Co ions.

As for the magnetic phase transition analysis of $Zn_{0.95-x}Mg_xCo_{0.05}O$ DMS structures, the observed temperature dependence in the temperature-dependent magnetization curves follows the typical behavior of paramagnetic materials with weak ferromagnetic interactions, having already discussed the experimental findings in Figs. 2 and 3. Further, no clear transition to a strong ferromagnetic phase is observed, reinforcing that $Zn_{0.95-x}Mg_xCo_{0.05}O$ DMS structures remain predominantly paramagnetic across the investigated temperature ranges.

3.1.2 ZFC-FC measurements of $Zn_{0.95-x}Mg_xCo_{0.05}$ bulk DMS structures

Figures 5–7 indicate the difference in the temperature-dependent magnetization curves for $Zn_{0.94}Mg_{0.01}Co_{0.05}O$, $Zn_{0.92}Mg_{0.03}Co_{0.05}O$, and $Zn_{0.90}Mg_{0.05}Co_{0.05}O$ structures annealed at 800 °C for 30 min in ZFC and under a 100 Oe applied magnetic field strength. All the semiconducting compounds exhibit distinct characteristics of the DMS structures. The figures also reveal that the samples present similar curves related to the magnetizations in ZFC and FC sequences. In more detail, the magnetization of both the ZFC and FC curves decreases as the ambient temperature increases due to the thermally activated demagnetization.

At low-temperature regions, the ZFC and FC magnetization curves exhibit a pronounced divergence as a result of the presence of magnetic anisotropy and possible spin-glass-like behavior. Besides, the considerable enhancement in magnetization curves at low-temperature regions implies the presence of ferromagnetic interactions among Co–Co magnetic ions, possibly mediated by carrier-induced exchange coupling based on the spin magnetic moment alignment, carrier concentration, electronic structure, intrinsic defects, oxygen vacancies, or structural defects. Moreover, in Figs. 5–7, the smooth reduction with enhancing ambient temperatures shows that thermal fluctuations weaken the alignment of magnetic moments and potential carrier-mediated ferromagnetic interactions, reducing net magnetization. The persistence of magnetization up to higher temperature regions scrutinizes that the $Zn_{0.95-x}Mg_xCo_{0.05}O$ DMS structures retain some magnetic ordering as a result of localized Co–O–Co interactions. According to the figures, the absence of a high Curie temperature reveals that the $Zn_{0.95-x}Mg_xCo_{0.05}O$ DMS structures do not undergo a well-defined phase transition; however, they show a gradual paramagnetic transition, as a consequence of the typical behavior of DMS systems.

We also determine the temperature-dependent magnetization curves at 300 K and 20 K under a 100 Oe applied magnetic field strength for all the Mg/Zn partially replaced ZnO semiconducting samples. It is obvious that all the DMS structures exhibit typical paramagnetic behavior, as seen in Fig. 8. Magnetization increases linearly with increasing magnetic field strengths. At room temperature, it means that the magnetic field can partially remove spin

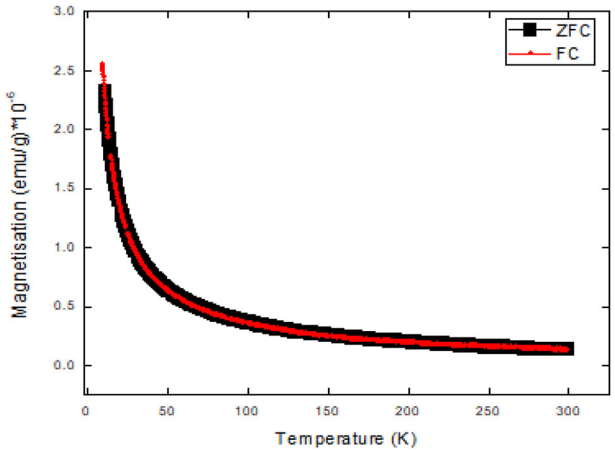

Fig. 6 Temperature variation of magnetization of $Zn_{0.92}Mg_{0.03}Co_{0.05}O$ at 800 °C for 30 min under 100 Oe applied magnetic field

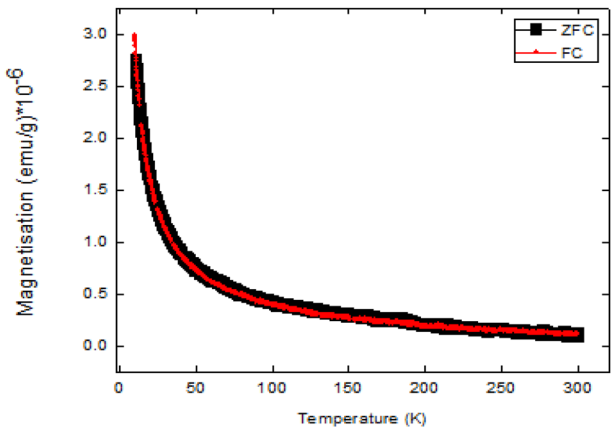

Fig. 7 Temperature variation of magnetization of $Zn_{0.94}Mg_{0.01}Co_{0.05}O$ at 800 °C for 30 min under 100 Oe applied magnetic field

degeneracy as well. A strong field aligns a significant number of free spins. Accordingly, the degeneration is partially eliminated, and consequently, the spin entropy reduces significantly, and large magnetothermo power is observed. In more detail, at lower temperatures, the temperature-dependent magnetization curves are noted to be significantly higher as a result of strong magnetic interactions. As the ambient temperature rises, the magnetization gradually decreases, which is characteristic of thermal energy overcoming magnetic ordering. Furthermore, the divergence between FC and ZFC curves indicates the presence of magnetic anisotropy, spin-glass behavior, or superparamagnetic effects. Especially, the deviation is observed to be more prominent at lower temperature regions, related to the possibility of frozen magnetic moments or weak ferromagnetic interactions (having already been discussed above). It is also seen that the change in the curves with the substitution level points out the variation of magnetic response depending on the Mg/Zn partial replacement mechanism. Figure 8 assesses the

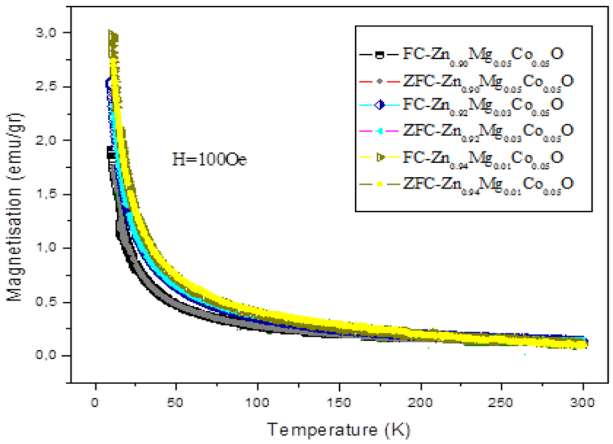

Fig. 8 Temperature variation of magnetization of $Zn_{0.95-x}Mg_xCo_{0.05}O$ samples under 100 Oe applied magnetic field

modification of the overall magnetization behavior under higher Mg ion concentration levels due to changes in carrier-mediated ferromagnetism or structural modifications affecting exchange interactions between doped ions and charge carriers in the semiconducting matrix. In the temperature region above 200 K, a flattening of the magnetization curves is observed, declaring a transition towards a paramagnetic state in which thermal fluctuations dominate over any intrinsic magnetic arrangement.

The plots given in Fig. 9 represent the magnetization as a function of the applied magnetic field strengths for $Zn_{0.95-x}Mg_xCo_{0.05}O$ DMS structures. Here, both zero-field-cooled and field-cooled magnetization curves are displayed, where the black solid lines correspond to ZFC and the red dashed lines correspond to FC data. It is observed that the magnetization increases almost linearly with the external magnetic field strengths in all plots as a result of predominantly paramagnetic response behavior. Similarly, the absence of noticeable saturation at high field strengths further confirms the paramagnetic nature of the $Zn_{0.95-x}Mg_xCo_{0.05}O$ DMS structures. Besides, the insets indicate a magnified view of the low-field regions, where a very small hysteresis loop is observed. The negligible coercivity confirms weak ferromagnetic interactions or the presence of spin-glass-like behavior. Figure 9 also points out that the red dashed line (FC magnetization) is found to be slightly higher than the black solid line (ZFC magnetization). Especially, this situation is much more seen in the low-field regions, verifying some degree of irreversible magnetic behavior due to spin-glass-like effects or weak ferromagnetic interactions. Additionally, according to the plots in Fig. 9, all four subplots show similar trends due to the insignificant alteration of the overall magnetic response. Numerically, magnetization hysteresis loops are measured for ZFC and FC at 5 K. M vs. H curves are shown for dw = 6, 7, 8, and 9 nm. For instance, at dw = 6 nm, a small coercivity of 230 Oe is observed in the ZFC curve and an almost linear shape in

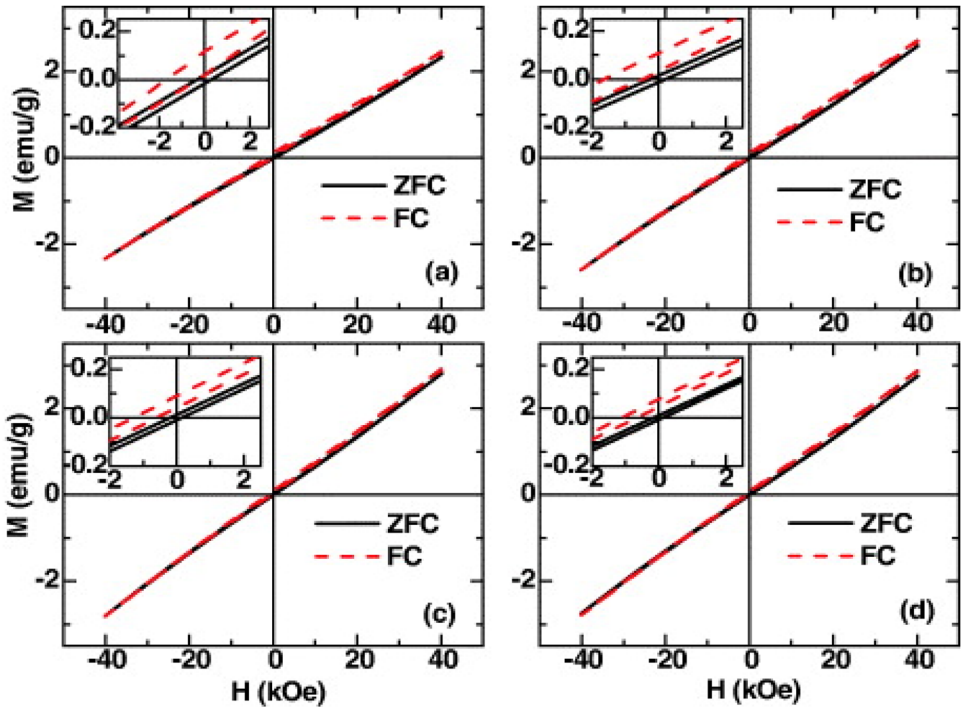

Fig. 9 *M* vs. *H* hysteresis curves at 5 K after ZFC and after FC in 40 kOe for $d_w = 5$ (**a**), 6 (**b**), 7 (**c**), and 9 nm (**d**). The insets show an enlarged view of the central part

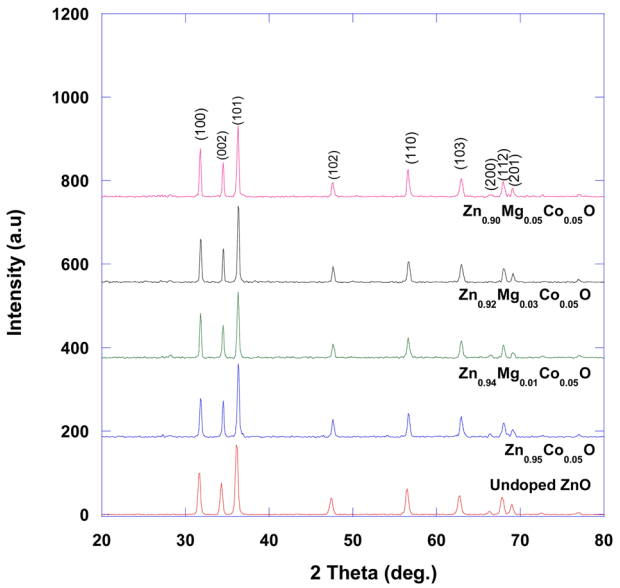

Fig. 10 XRD patterns of samples

$H < 40$ kOe. The hysteresis curves are obtained under a 40 kOe applied field in the FC condition, revealing an increase in the coercive field to 570 Oe. Consequently, a vertical shift towards higher M(H) values is observed. A horizontal shift occurs depending on the vertical shifts. It should not be understood as exchange bias. On the contrary, this behavior of the M (H) curve is found to be in harmony with hysteresis curves observed on Diluted-Antiferromagnetic (DAF) systems. $Zn_{0.95-x}Mg_xCo_{0.05}O$ DMS structures with different sizes qualitatively exhibit similar behavior (Fig. 9).

3.2 Structural properties

3.2.1 XRD analysis for $Zn_{0.95-x}Mg_xCo_{0.05}O$ DMS structures

X-ray diffraction analysis is conducted to examine the structural quality and crystallographic characteristics of $Zn_{0.95-x}Mg_xCo_{0.05}O$ DMS structures (Fig. 10). The XRD patterns for all samples reveal the characteristic ZnCoO crystal structure with a preferential orientation along the 100, 002, and 101 diffraction planes. As shown in Fig. 10, no secondary phases related to Mg^{2+} ions are observed, suggesting successful substitution of Zn^{2+} ions in the host lattice without disrupting the wurtzite crystal structure. This can be attributed to the successful replacement of Zn^{2+} (0.74 Å) ions with foreign impurity ions, Co^{+2} (0.70 Å) and Zn^{2+} (0.72 Å), without altering the original crystal structure [27, 28]. Furthermore, the incorporation of impurity ions into the crystal lattice leads to slight shifts in the diffraction peaks to lower or higher 2θ angles, differentiation in diffraction intensities, broadening or narrowing of the full width at half maximum (FWHM), and reflecting the modification of the crystal system. The diffraction peaks are indexed according to Miller indices *hkl*, as seen in Fig. 10. Both the SEM investigation images and XRD characteristic peaks indicate that the presence of Mg and Co ions in the crystal system does not impair the characteristic hexagonal

wurtzite structure of ZnO semiconductor. Notably, the *002* diffraction peak shows a regular shift to greater 2θ angles with increasing Mg impurity ion concentrations. Besides, these kinds of shifts for 2θ angles are also observed for the *101* and *102* characteristic diffraction peaks. It is well known that the shifts observed in diffraction peak positions are attributed to changes in lattice parameters due to the differences in ionic radius and electronegativity between the dopants (Co^{+2} and Mg^{2+}) and the host Zn^{2+} ions. In particular, the partial replacement of Zn^{2+} by the smaller Co^{+2} and Mg^{2+} ions leads to lattice contraction, shifting the peaks to higher angles. In summary, the relatively small difference in ionic radii between Zn^{2+} and the foreign dopant ions (Co^{2+} and Mg^{2+}) adequately accounts for the slight reduction in lattice parameters observed with increasing Mg/Zn substitution in the ZnCoO semiconductor matrix.

Moreover, the existence of Mg ions in the semiconducting matrix results in an increase in the intensity of the characteristic *002* peak relative to the undoped ZnCoO system. Similarly, the magnesium impurity supports the growth of *100* diffraction peaks in the XRD diffractograms. The recorded changes in diffraction peak intensities and peak positions further reveal that the substitution of foreign Co^{+2} and Mg^{2+} ions for host Zn^{2+} ions results in a reorganization of the typical hexagonal wurtzite ZnO lattice system. This structural modification may lead to the formation of additional interface states on the ZnO surface, which could be advantageous for real-world technological applications, including spintronics and magneto-optoelectronic devices.

Furthermore, it can be argued that the incorporation of impurity dopant ions somewhat influences the distribution of energy levels within the energy bandgap by affecting charge carrier transport, electron transfer kinetics, and the fundamental reactivity and stability of the material. Even magnetization experiments conducted under varying temperatures and applied magnetic field strengths have already corroborated these findings. The FWHM of characteristic diffraction peaks in the Mg/Zn partially replaced semiconducting system is smaller than that of the undoped one. This confirms that Mg/Zn substitution improves the material crystallinity, which has already been confirmed by the SEM investigations. Therefore, Mg foreign ions may be preferred for stabilizing the crystal structure.

Moreover, the crystallite sizes of $Zn_{0.95-x}Mg_xCo_{0.05}O$ DMS structures are determined from the most intense diffraction peaks using the Warren–Scherrer equation [29]:

$$d = 0.941\lambda/B\cos\theta_B \quad (1)$$

where d represents the crystallite size, λ is the X-ray wavelength (1.54 Å), β denotes the full width at half maximum (FWHM) of the peak, and θ refers to the Bragg angle of the XRD peak. The computed grain sizes for all semiconducting samples investigated are summarized in Table 1. As shown in the table, the crystallite size exhibits a slight reduction from 37.62 nm in the $Zn_{0.95}Co_{0.05}O$ structure to 36.48 nm in the bulk $Zn_{0.90}Mg_{0.05}Co_{0.05}O$ compound. The bulk $Zn_{0.92}Mg_{0.03}Co_{0.05}O$ semiconductor possesses an average grain size of 37.10 nm, while the $Zn_{0.94}Mg_{0.01}Co_{0.05}O$ material presents an average crystallite size of 37.22 nm. The variations in crystallite size with dopant substitution can be explained by the differences in electronegativity and ionic radii between the dopants (0.70 Å of Co^{+2} and 0.72 Å of Mg^{2+}) and the host Zn^{2+} (0.74 Å) ions in the ZnO matrix without disrupting the hexagonal wurtzite structure. The partial substitutions of Zn^{2+} ions with smaller Co^{+2} and Mg^{2+} ions result in a decrease in average crystallite size. Accordingly, it can be concluded that the incorporation of Mg impurities into the $Zn_{0.95-x}Mg_xCo_{0.05}O$ DMS system enhances crystallization and strengthens particle couplings within the crystal structure. This effect is attributed to the presence of closer neighboring atoms, which promote stronger interparticle bonding, the formation of new chemical bonds, and enhanced interactions between adjacent atomic groups [12, 30]. Consequently, all Mg/Zn partially replaced ternary ZnCoO semiconductors exhibit enhanced structural integrity. These structural improvements are experimentally evidenced by the SEM images and APS value.

Furthermore, it is important to highlight that the reduction in crystallite size leads to pronounced quantum confinement effects when the crystallite dimensions become comparable to the electron wavelength [31, 32]. The interplay between reduced crystallite size and increased defect states further amplifies these effects in ZnCoO-based materials. Consequently, this physical phenomenon significantly enhances the potential of ZnCoO-based materials for real-world technological applications.

3.2.2 Detailed SEM investigations for Mg/Zn partially substituted $Zn_{0.95-x}Mg_xCo_{0.05}O$ diluted magnetic semiconductors

Detailed SEM analyses are performed to support the fundamental magnetic (ferromagnetic/paramagnetic/superpara magnetic behavior, magnetic response, defect-mediated exchange interaction magnetism, thermal fluctuations, coercivity, magnetothermo power, thermal activation of localized magnetic moments, stabilization in susceptibility, thermally activated demagnetization, defect/carrier-mediated ferromagnetic interactions, Co–Co magnetic interactions, short-range magnetic correlations, magnetic anisotropy, spin-glass-like behavior, spin degeneracy, spin entropy, Curie temperature, spin magnetic moment alignment, charge carrier concentration, electron density, and oxygen vacancies) and micromechanical test results

Table 1 Mechanical parameters calculated from the loading–unloading curves for all the samples

Samples	Load (mN)	Contact Depth (μm)	Hardness (GPa)	Indentation modulus (GPa)	Grain Size (nm)
$Zn_{0.95}Co_{0.05}O$	400	31.231	0.0162	0.575	37.62
	800	15.901	0.0269	0.827	
	1200	35.075	0.0389	1.952	
	1600	38.506	0.0432	2.518	
	2000	30.288	0.0648	4.417	
$Zn_{0.94}Mg_{0.01}Co_{0.05}O$	400	15.112	0.0872	1.757	37.22
	800	19.838	0.0828	2.370	
	1200	25.091	0.0784	3.521	
	1600	26.811	0.0706	4.738	
	2000	35.400	0.0690	6.463	
$Zn_{0.92}Mg_{0.03}Co_{0.05}O$	400	23.576	0.0280	0.772	37.10
	800	26.906	0.0444	1.094	
	1200	33.812	0.0420	1.236	
	1600	27.910	0.0828	3.297	
	2000	32.343	0.0766	4.275	
$Zn_{0.90}Mg_{0.05}Co_{0.05}O$	400	15.566	0.0670	1.468	36.48
	800	16.297	0.0771	2.246	
	1200	30.659	0.0708	1.295	
	1600	30.277	0.0694	2.081	
	2000	36.801	0.0922	2.914	

(interactions between hexagonal layers, resistance to external forces, crack orientation/geometry, grain boundary problems, intergranular interactions, stored internal strain energy for crack propagation, AOSSm, D/DG, SRCSa, AFB, and n-RSAa within the matrix). The resulting micrographs provide insight into the mechanisms of how the substitution process affects the crystal structure, surface morphology, and fundamental microstructural features. Particular aspects investigated include grain alignment distributions, particle growth, uniformity, layer formation, microcrystal orientations, micropores, microcrystal coalescence, voids, cracks, partially melted regions, and grain boundary coupling interaction problems. As a result, key structural modifications at critical substitution levels are identified, allowing for a more comprehensive analysis of the surface morphology. Figure 11a–d presents SEM images captured at 100,000× magnification with an accelerating voltage of 10 kV in SEI mode for $Zn_{0.95-x}Mg_xCo_{0.05}O$ diluted magnetic semiconductors. The experimental surface images indicate that the substitution mechanism slightly impacts crystallinity, surface morphology, and microstructural features of newly modified $Zn_{0.95-x}Mg_xCo_{0.05}O$ DMS structures. The images reveal alterations in surface morphology as a function of Zn/Mg concentrations. The substitution mechanism is noted to control the orientations and size of the newly modified structures. Besides, the newly synthesized semiconducting materials possess hexagonal structures with average diagonals (diameter) below 100 nm in a one-dimensional configuration. The grains, exhibiting a non-uniform particle distribution and arrangement, are dispersed across randomly oriented surfaces while retaining their hexagonal shape and smooth texture. The presence of foreign impurity ions in the bulk $Zn_{0.95-x}Mg_xCo_{0.05}O$ structures leads to a slight morphological transformation. In this respect, all the semiconducting materials almost completely preserve their original hexagonal wurtzite crystal structure morphology.

With an increase in Mg/Zn substitution concentration, the grain size distribution decreases gradually. The change in diameters with the substitution mechanism can be attributed to the interaction between the incorporated magnesium atoms and the surrounding atoms within the host crystal structure. Magnesium atoms integrate more readily with neighboring zinc or oxygen atoms due to the lower energy required for bond formation during the orbital interaction process. Consequently, the replacement mechanism in wurtzite-type ZnCoO semiconductors varies the crystal structure quality and influences nanorod diameter growth. In other words, a substantial decrease in diameters is achieved with the incorporation of foreign impurity atoms. Besides, the different ionic radius of substitution ions (the ionic radius of host Zn^{+2} is 0.74 Å while the ionic radii for the Co^{+2} and Mg^{+2} are 0.70 Å and 0.72 Å, respectively) may be responsible for the slight reduction of diameters [33–36]. Furthermore, the incorporation of magnesium into the $Zn_{0.95-x}Mg_xCo_{0.05}O$ matrix may promote the formation of new bonds or chemical interactions between

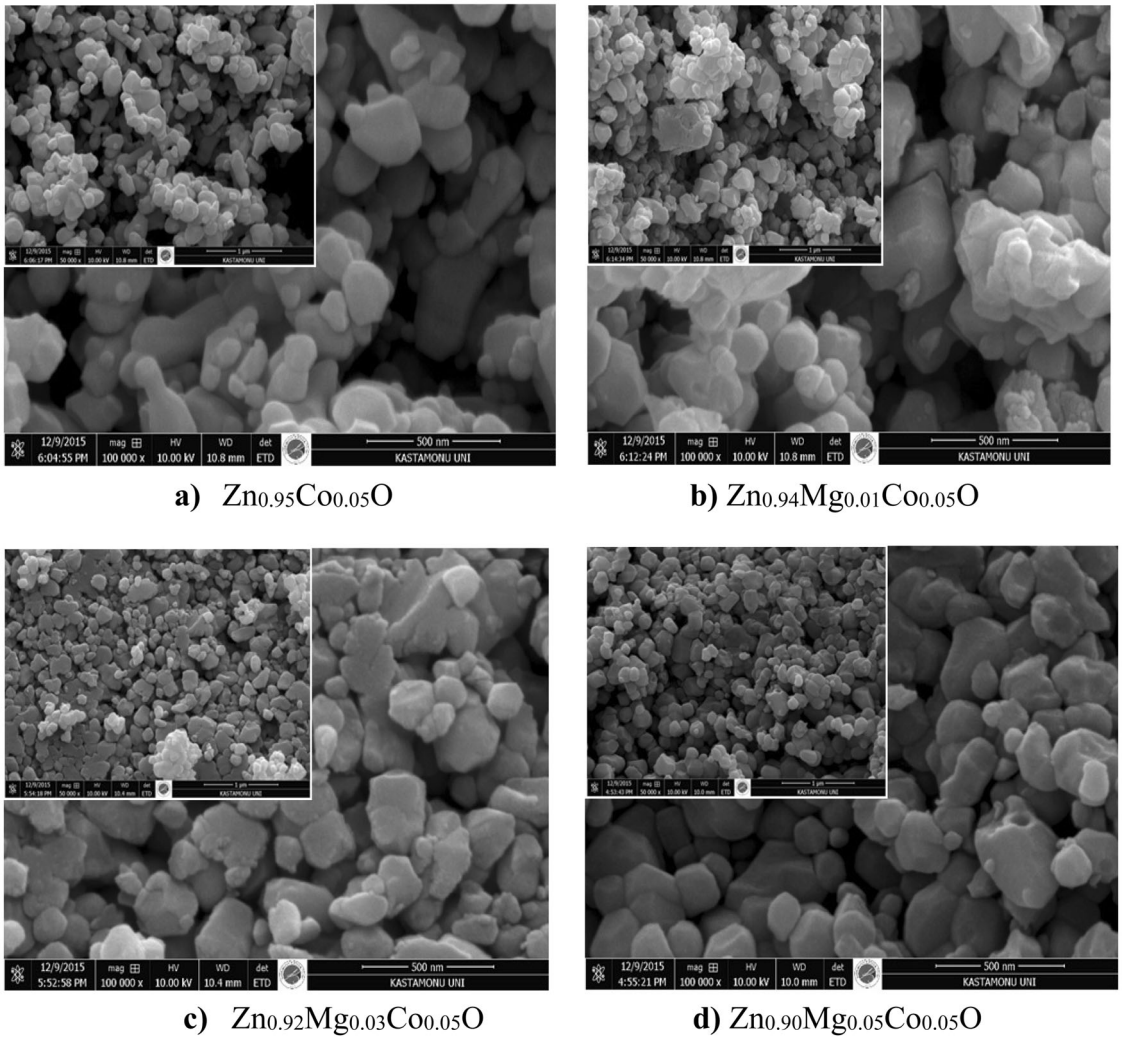

Fig. 11 SEM images of **a** Zn0.95Co0.05O; **b** Zn0.94Mg0.01Co0.05O; **c** Zn0.92Mg0.03Co0.05O; **d** Zn0.90Mg0.05Co0.05O

adjacent atomic groups due to their increased proximity. On the other hand, a gradual decrease in the average diameter of samples studied indicates that Mg incorporation may inhibit the crystal growth of ZnCoO DMS structures along the preferential direction due to a random increase in roughness. The reduction trend in the (thicker) particle sizes is a positive development for mechanical hardness characteristics. This is also attributed to the enhanced magnetizations due to the refinement in the defect-mediated exchange interaction magnetism. It is well known that the differentiation in the crystal structure based on the substitution mechanism affects the uniformity of charge distribution, particle size dimensions/distributions, interspacing, composition, and thickness of the ZnO layer. According to Fig. 11, the surface morphologies of all the compounds consist of granular formations with multiple grain clusters exhibiting varying sizes and distributions. The bulk $Zn_{0.95}Co_{0.05}O$ semiconducting structure exhibits a granular and porous microstructure characterized by irregularly distributed voids on the sample surface. It is well known that porosity significantly influences both the physical and functional properties of ZnO structures. Physically, high porosity reduces the mechanical strength, density, and hardness of the semiconducting material due to the presence of voids and microcracks that serve as stress concentrators and crack initiation sites. This leads to decreased resistance to external forces and diminished load-carrying capacity. Functionally, porosity alters the electrical, optical, and magnetic behavior of ZnO by disrupting charge carrier mobility, enhancing surface defect states, and modifying light scattering pathways. Therefore, there is a significant correlation between morphology and electrical properties. Accordingly, in electronic and optoelectronic applications, excess porosity can reduce carrier concentration and conductivity by introducing scattering centers and charge traps, thereby degrading device efficiency. On the other hand, in engineering applications such as gas sensing or photocatalysis, controlled porosity is beneficial due to the enhanced surface

area, adsorption sites, and reactivity. Therefore, while moderate, tailored porosity may enhance certain surface-dominated functionalities, excessive or uncontrolled porosity generally compromises the structural integrity and key mechanical performance of ZnO-based materials. As shown in Fig. 11a, an increase in the average grain diameter and a broader size distribution are observed. The reduction in crystalline size is evident in Fig. 11b, where the $Zn_{0.94}Mg_{0.01}Co_{0.05}O$ DMS structure presents irregularly distributed voids. With further decrease in particle sizes based on the Mg/Zn partial substitution amounts, tightly bound grain clusters and more distributions are displayed for the $Zn_{0.92}Mg_{0.03}Co_{0.05}O$ structure. Accordingly, the smoothest surface image is obtained. This is because Mg/Zn substitution contributes to the improvement of the crystallinity of the material. However, the surface morphology underwent a significant transformation, reverting to a nanoporous structure in the $Zn_{0.90}Mg_{0.05}Co_{0.05}O$ composition. All the SEM measurement findings are supported by the XRD experimental results (Table 1).

Integrating magnetization measurements with SEM imaging, the reduction in particle size distribution within the semiconducting matrix, attributed to magnesium incorporation, appears to influence carrier concentration, electron density, and the formation of structural defects.

We also evaluate average particle size (APS) evolution in the $Zn_{0.95-x}Mg_xCo_{0.05}O$ matrices to assess the influence of partial Mg substitution amount using SEM investigations in conjunction with the ImageJ software for quantitative evaluation. SEM micrographs revealed that Zn doping substantially affects the grain structure, particularly the particle size and its distribution within the surface morphology. Figure 12a, b illustrates the stepwise procedure for APS estimation, while the corresponding quantitative results are provided in Fig. 12c. The data indicate that the APS number is found to decrease considerably upon the incorporation of a quantity of Mg ions. On this basis, the APS are determined to be about 205.064 ± 39.027 nm, 196.009 ± 36.230 nm, 165.038 ± 26.282 nm, and 150.553 ± 36.691 nm for the $Zn_{0.95}Co_{0.05}O$, $Zn_{0.94}Mg_{0.01}Co_{0.05}O$, $Zn_{0.92}Mg_{0.03}Co_{0.05}O$, and $Zn_{0.90}Mg_{0.05}Co_{0.05}O$ semiconducting materials, respectively. The decrement trend with the Mg/Zn replacement level is related to the improved crystallization kinetics and increased linkage between the atoms, which promote the formation of a denser, more homogeneous surface microstructure. However, the rapid decrement in the APS value but increase in the standard deviation for the $Zn_{0.90}Mg_{0.05}Co_{0.05}O$ compound stems from the nanoporous structure. Besides, the APS parameters provide valuable information about the variation of magnetization and mechanical hardness characteristics of semiconducting materials. Accordingly, the $Zn_{0.92}Mg_{0.03}Co_{0.05}O$ sample with the optimum APS value exhibits the highest mechanical performance features, being already confirmed by the following sections. The optimized microstructure is further characterized by enhanced grain coupling, larger and more uniformly distributed particles (due to lower standard deviation), and superior alignment of microcrystalline domains, which are directly linked to enhanced mechanical performance.

3.3 Mechanical properties

The influence of the Mg/Zn partial substitution mechanism on the key micromechanical performance features of ZnO-based DMS nanostructures is extensively investigated by instrumented indentation tests performed under external load intervals 0.5 N–2.0 N. In conventional microhardness analysis, an indenter is pressed onto the sample surface, and the diagonal lengths of the indentation are measured after the load is removed. Microhardness values are then calculated based on the experimental measurements. In the instrumented indentation technique, all parameters can be determined, taking into account indenter depth and load during elastic/plastic deformation.

A technique introduced by Oliver and Pharr in 1992 enables the determination of elastic modulus and microhardness from the loading–unloading curve, providing more accurate results compared to conventional static indentation methods. Figure 12 illustrates a schematic representation of the indentation load-contact depth curve along with a cross-sectional diagram of an indentation.

As shown in Fig. 13a, the loading phase can be described as follows:

$$F = Ch^m \tag{2}$$

where F and h are the applied load and contact depth, respectively. m and C are the indenter constants (Fig. 13b). For cones, the m index is 2.

$$F = a\,(h - h_0)^m \tag{3}$$

here, h_0 is the final contact depth when the constants a and m are indenter parameters. The contact stiffness is given as follows. The fitted unloading curve is calculated by

$$S = \left|\frac{dF}{dh}\right|_{F_{\max}} = ma(h - h_0)^{m-1} \tag{4}$$

and contact depth can be given as follows

$$h_c = h_{\max}\varepsilon\frac{F_{\max}}{S} = h_{\max}\varepsilon\frac{F_{\max}}{dF/dh} \tag{5}$$

ε is the contact parameter (0.75 for the Vickers indenter). During indentation, the indenter deformation can be

obtained using the reduced modulus given as Eq. 5. The modulus is calculated from the slope of the unloading curve at F_{max}.

$$E_r = \frac{\sqrt{\pi}}{2\beta\sqrt{A_c}} \tag{6}$$

where A_c and β are the area of the indent and a contact parameter, respectively. The indentation modulus can be calculated as follows.

$$\frac{1}{E_r} = \frac{1-\vartheta^2}{E} + \frac{1-\vartheta_i^2}{E_i} \tag{7}$$

E and υ, Young's modulus and Poisson's ratio, E_i and υ_i, are the same parameters for the indenter. Hardness values are calculated by Eq. 7.

$$H = \frac{F_{max}}{A_c} \tag{8}$$

Figure 12a–f indicates load-contact depth curves of Mg and Co-doped ZnO semiconducting structures. In addition, the F, H_v, and indentation modulus values of all samples are numerically summarized in Table 1. The figures also enable us to determine the general mechanical characteristics of bulk semiconducting samples. Namely, the phenomenon where the microhardness value decreases as the applied test load increases is referred to as the Indentation Size Effect (ISE). In contrast, the phenomenon where an increase in the applied load leads to a rise in hardness is known as the Reverse Indentation Size Effect (RISE) behavior [37, 38]. As can be seen from the table, the microhardness values for the $Zn_{0.95}Co_{0.05}O$ semiconducting structure increase with increasing applied loads from 400 mN to 2000 mN. This result shows that the microhardness parameters enhance with increasing applied test loads due to the untypical RISE mechanical behavior. However, the presence of the non-magnetic magnesium ions in the semiconducting system varies inversely with the mechanical characteristic behavior of the bulk $Zn_{0.94}Mg_{0.01}Co_{0.05}O$ DMS structure. On this basis, the $Zn_{0.90}Mg_{0.05}Co_{0.05}O$ and $Zn_{0.92}Mg_{0.03}Co_{0.05}O$ materials exhibit the typical ISE nature under applied test loads. The change in the mechanical characteristic behavior confirms the successful integration of the Mg impurity ions into the lattice systems. According to the table, the $Zn_{0.95}Co_{0.05}O$ semiconducting structure exhibits the minimum hardness parameters at any applied test loads due to the granular and porous microstructure (Table 1), having already been verified by the SEM images and APS value. When maximum load was applied, the large differences in the depth occurred [39]. Conversely, the enhancement in microhardness parameters can be attributed to increased crystallinity and the formation of tightly bound grain clusters. Additionally, the reduced intergranular spacing, along with the formation of new chemical bonds and interactions between adjacent atomic groups, further reinforces the microhardness properties. On the other hand, the $Zn_{0.90}Mg_{0.05}Co_{0.05}O$ material exhibits distinct mechanical behavior, which is believed to result from the re-formation of a nanoporous structure on the specimen surface. This observation is further corroborated by the standard deviation values of the APS data, which quantitatively confirm the variations in particle size distribution and substantiate the microstructural inhomogeneity at the highest Mg substitution level. It is also observed that the idea of Mg/Zn substitution clearly enhances the key mechanical performance properties of bulk $Zn_{0.95-x}Mg_xCo_{0.05}O$ DMS structures due to the enhancement in the resistance to external forces, intergranular interactions, AOSSm, D/DG, SRCSa, AFB, and n-RSAa based on the decreased crack orientation/geometry, grain boundary problems, and stored internal strain energy for crack propagation within the matrix. Shortly, the existence of impurity ions stabilizes the $Zn_{0.95-x}Mg_xCo_{0.05}O$ DMS structures. Magnesium ions function as artificial barriers, restricting dislocation mobility and crack propagation while optimizing internal strain energy. Consequently, the critical stress required for deformation increases, enhancing the fundamental mechanical stability of the bulk $Zn_{0.95-x}Co_{0.05}O$ DMS structure.

Moreover, as confirmed by SEM image analysis, structural enhancements with the substitution mechanism contribute to notable improvements in structural, magnetic, and key mechanical performance quantitates. The magnesium ion concentration stabilizes the non-recoverable stress amplified areas by forming new AFB, AOSSm, and SRCSa regions on the surface, improving material stability, durability, and structural integrity under applied loads. The enhancements strengthen intergranular interactions, further reinforcing key mechanical performance properties.

In particular, the presence of foreign impurities seems to fortify chemical bonds and enhance intergranular interactions between non-magnetic Mg particles and host matrix ions in the ZnMgO semiconducting system, as confirmed by SEM experimental results. This leads to a $Zn_{0.95-x}Mg_xCo_{0.05}O$ DMS structure with superior resistance to external test forces, corrosion, and fatigue. Among all tested samples, the pure $Zn_{0.95}Co_{0.05}O$ material exhibits the highest sensitivity to applied test loads, indicating inferior mechanical performance. However, in the case of Mg/Zn substitution, the crystallinity improvement, favorable crack orientation, improved grain boundary coupling, and decreased deformation become evident. The findings discussed are further supported by SEM analysis, confirming the advantageous effects of Mg/Zn partial substitution on the semiconducting system.

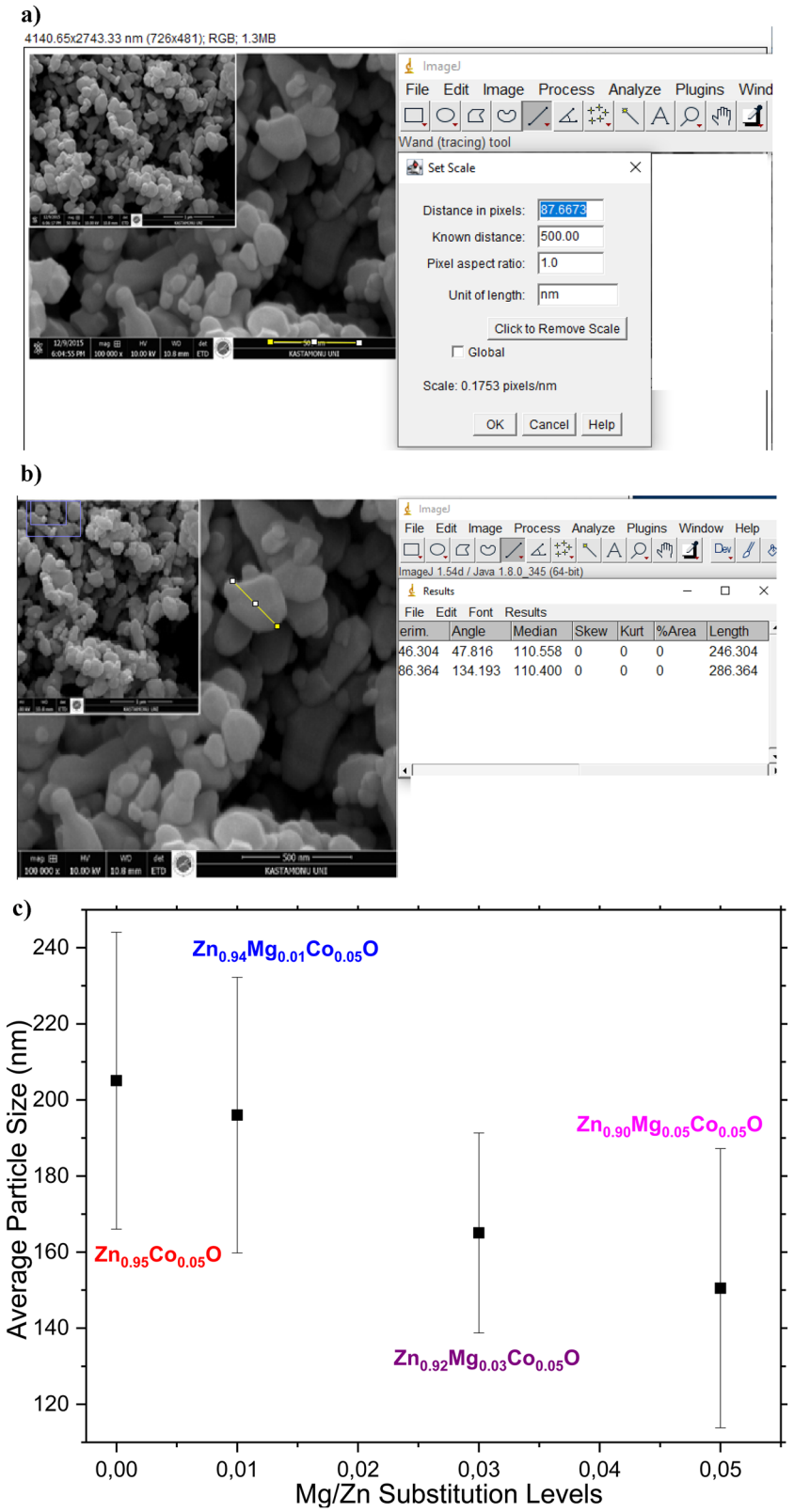

Fig. 12 **a** Calculation method for average particle size parameters and working principle for ImageJ software program, and **b** variation of APS parameters for $Zn_{0.95-x}Mg_xCo_{0.05}O$ nanoparticles using ImageJ software program

Numerically, Co-doped ZnO exhibits the lowest peak indentation depth of 30.288 µm, whereas the $Zn_{0.90}Mg_{0.05}Co_{0.05}O$ sample with 5% Mg ion replacement shows the highest peak depth of 36.801 µm at a maximum load of 2000 mN. This variation is strongly correlated with microstructural modifications, including a reduction in grain

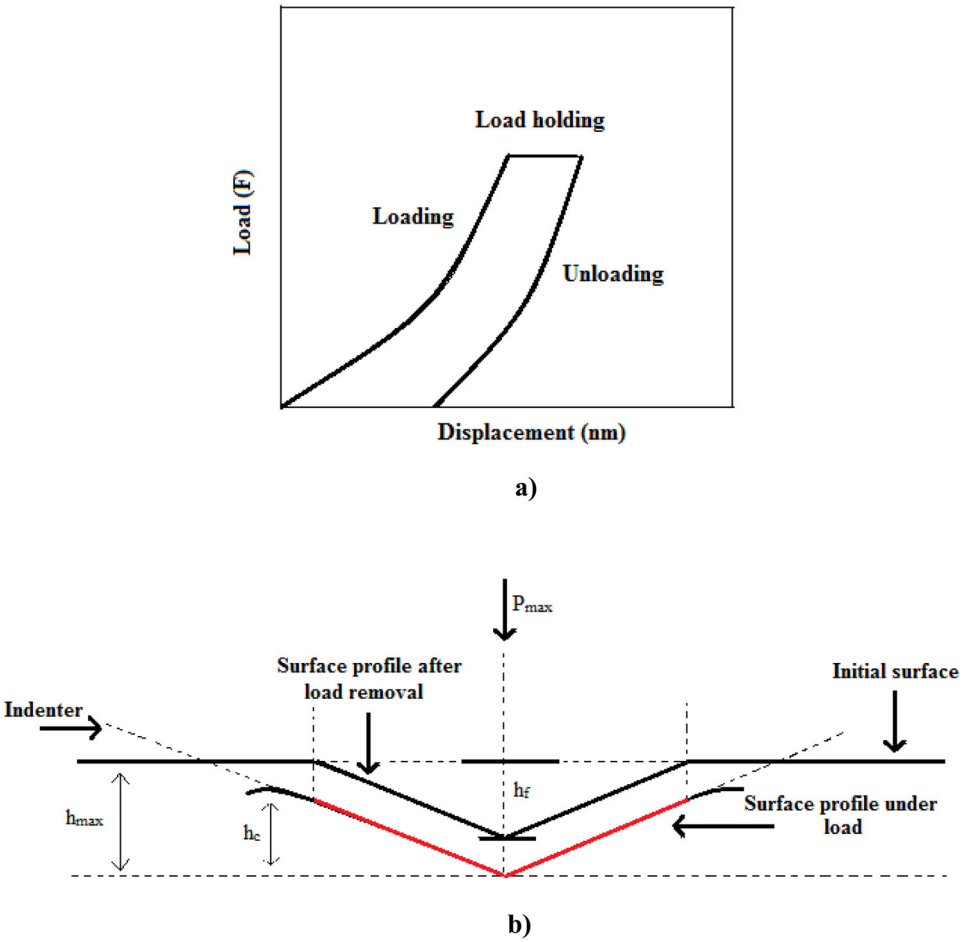

Fig. 13 **a** Schematic diagram of indentation load- contact depth curve. **b** A cross-sectional diagram of an indentation

size, variations in lattice parameters, and decreased porosity. A reduction in grain size is often associated with increased hardness, a trend widely reported in the literature [40–42]. Therefore, it can be concluded that Mg/Zn substitution induces significant microstructural changes in ZnO, directly influencing the hardness of the samples.

All samples exhibit creep behavior, as observed in the loading–unloading curves. This phenomenon is defined as time-dependent deformation occurring during indentation [43]. During the application of the applied test load, the indenter continues to penetrate the sample, increasing the indentation area, as illustrated in Fig. 14 [44, 45]. The extent of indentation creep depends on numerous factors, such as the material type, applied load, loading rate, and load duration [46]. Creep behavior is quantified by measuring the change in indentation depth throughout the test duration [3].

Additionally, all $Zn_{0.95-x}Mg_xCo_{0.05}O$ DMS structures display a pop-in event, which is observed in the loading segment of the loading–unloading curves. A pop-in event refers to an abrupt displacement or sudden increase in load during indentation. If a similar event occurs during the unloading phase, it is referred to as a pop-out event [47]. While a pop-in event is detected in Fig. 14a, it is not observed in other samples. Furthermore, no pop-out events are recorded in the indentation cycles of any samples.

Defects in the microstructure and dislocation of cracks under an applied load can contribute to the occurrence of pop-in events [48–50]. As shown in Fig. 14b–d, no pop-in events are observed in Mg-doped nanoparticles. This finding suggests that Mg/Zn partial substitution plays a crucial role in preventing mechanical alterations by influencing the crystal structure of the bulk ZnCoO structure.

The elastic (indentation) modulus can be determined from the loading–unloading curves obtained in microhardness tests [51]. The summarized values are presented in Table 1 in detail. The results observed indicate that the load-dependent elastic modulus increases with increasing applied test loads. Additionally, the modulus increases up to a Mg/Zn replacement concentration of 1%, reaching its highest value of 6.463 GPa at 2000 mN. However, at a Mg concentration of 3%, the elasticity of the bulk ZnCoO semiconducting compound plateaus and subsequently decreases at higher doping levels. This trend confirms that excessive Mg substitution ions lead to increased plastic deformation rather than elastic deformation.

The microstructure of the $Zn_{0.95-x}Mg_xCo_{0.05}O$ DMS is a critical factor influencing microhardness. The grain size values

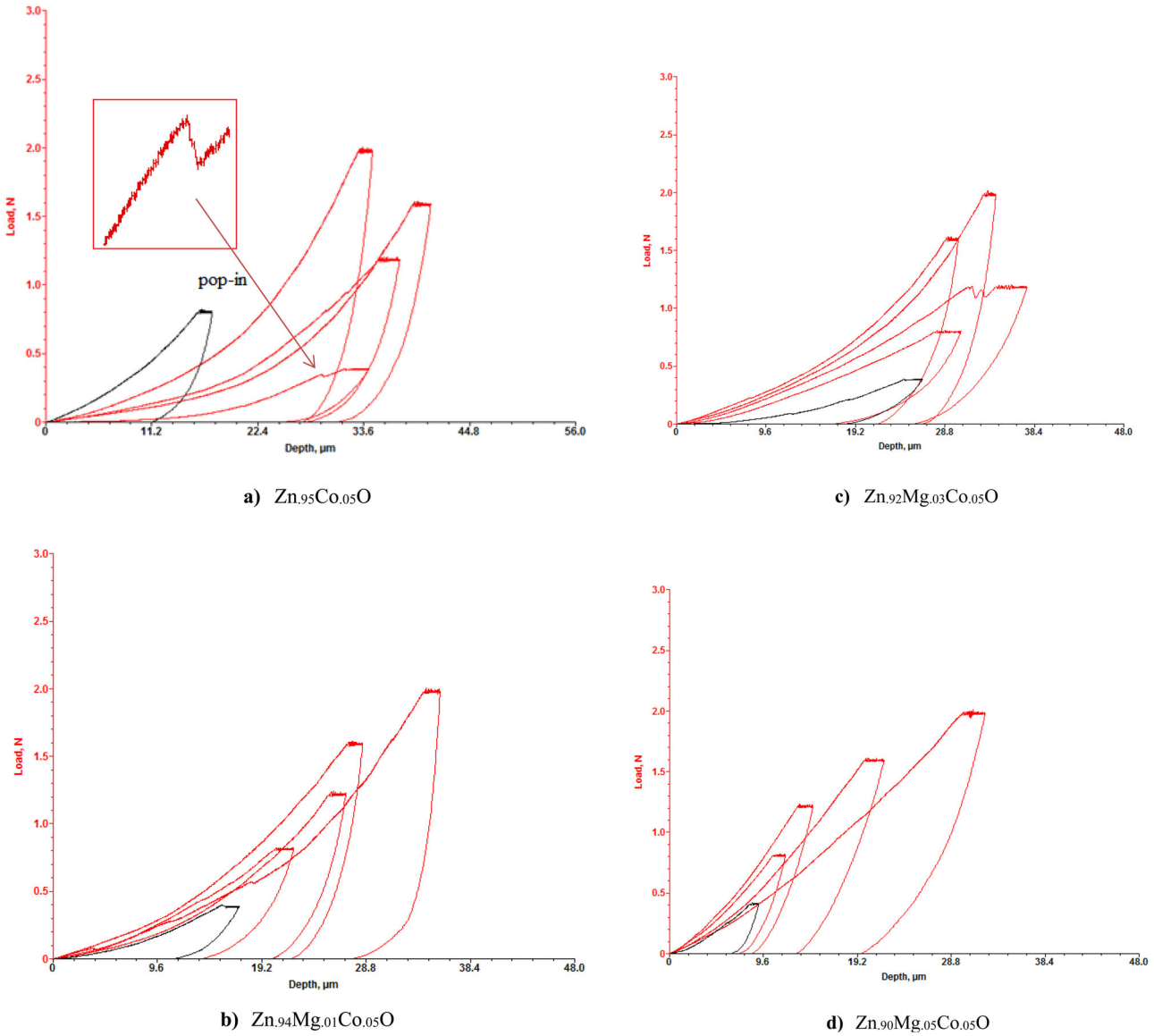

Fig. 14 Load-contact depth curves for **a** Zn0.95Co0.05O; **b** Zn0.94Mg0.01Co0.05O; **c** Zn0.92Mg0.03Co0.05O; **d** Zn0.90Mg0.05Co0.05O samples

decrease with increasing Mg/Zn substitution levels, leading to higher microhardness values. This increase in microhardness parameters can be attributed to the reduced intergranular spacing and enhanced grain connectivity between hexagonal layers with higher Mg/Zn replacement content. Stronger grain bonding enhances resistance to crack formation, suggesting that impurities at the grain boundaries contribute to the resistance of the material against mechanical failure [52].

4 Conclusions

In the current work, we examine the refinements in the structural, magnetic, and key mechanical performance features of bulk $Zn_{0.95}Co_{0.05}O$ DMS structures with Mg/Zn partially substitution mechanism with the aid of XRD, SEM, VSM, and H_v test measurements. All the experimental and calculation results confirm the successful integration of the Mg impurity ions into the bulk ZnCoO lattice systems. Mechanical hardness measurements reveal that Mg/Zn substitution enhances the mechanical properties of bulk $Zn_{0.95-x}Mg_xCo_{0.05}O$ DMS structures by reducing crack propagation, improving grain boundary integrity, minimizing internal strain energy, and stabilizing stress-concentrated regions. The incorporation of impurity ions increases resistance to external forces, corrosion, and fatigue while optimizing structural parameters such as AOSSm, D/DG, SRCSa, AFB, and n-RSAa. Magnesium ions act as artificial barriers, restricting dislocation mobility and inhibiting crack propagation, thereby optimizing internal strain energy distribution. This results in higher critical stress

thresholds for deformation, enhancing mechanical durability and stability. Additionally, SEM analysis confirms that Mg incorporation strengthens chemical bonding and intergranular interactions. Microhardness testing also indicates that $Zn_{0.95}Co_{0.05}O$ exhibits standard ISE behavior, whereas $Zn_{0.94}Mg_{0.01}Co_{0.05}O$ structure displays unconventional RISE behavior. The hardness curves reveal that among all samples, pure $Zn_{0.95}Co_{0.05}O$ semiconductor is the most sensitive to applied loads, demonstrating weaker mechanical performance. In contrast, Mg/Zn substitution improves crystallinity, optimizes crack orientation, enhances grain boundary coupling, and reduces deformation, contributing to superior mechanical stability.

SEM analysis reveals that Mg/Zn substitution affects charge distribution uniformity, particle size, interspacing, composition, and ZnO oxide layer thickness while preserving the hexagonal wurtzite structure and granular morphology. Increasing Mg/Zn concentration leads to a gradual reduction in grain size distribution, attributed to differences in electronegativity and ionic radii between dopants and host ions in the ZnCoO matrix. Magnesium incorporation likely facilitates new chemical interactions between adjacent atomic groups due to their closer proximity. Consequently, Mg/Zn-substituted structures exhibit smoother surface morphology and enhanced crystallinity, resulting from tightly bound and uniformly distributed grain clusters.

XRD analysis confirms the successful substitution of Zn^{2+} ions in the host lattice by Mg^{2+} ions without forming secondary phases, preserving the wurtzite crystal structure. The incorporation of Mg causes slight shifts in diffraction peaks, changes in peak intensities, and variations in FWHM values due to the formation of additional interface states on the ZnCoO surface. The modifications arise from differences in ionic radius and electronegativity between Mg^{2+} and Zn^{2+} ions. Mg/Zn substitution slightly reduces crystallite size from 37.62 nm to 36.48 nm by increasing the substitution levels. This incorporation enhances crystallization, strengthens atomic interactions, and improves particle coupling within the crystal structure, promoting quantum confinement effects. Further, the *M–H* curves indicate that in all the compounds studied, there appears to be a predominantly linear magnetic response at any temperature value, confirming that the dominant magnetic contribution is paramagnetic. It is noted that Mg/Zn substitution mainly affects electronic structure, oxygen vacancies, and defect-mediated exchange rather than directly enhancing magnetization. In more detail, the results show a predominantly paramagnetic response with negligible hysteresis, indicating weak or absent long-range ferromagnetic ordering. A slight magnetization increase at lower temperature ranges indicates weak defect-mediated ferromagnetic coupling, while thermal fluctuations at higher temperature ranges reinforce Curie–Weiss paramagnetism.

Additionally, the χ value decreases with temperature, stabilizing beyond 200 K. Conversely, higher χ values at lower temperatures indicate localized magnetic interactions. Besides, magnetization curves display DMS behavior with low-temperature divergence due to magnetic anisotropy and spin-glass effects. Weak ferromagnetic interactions among Co ions arise at low temperatures, likely through carrier exchange coupling. Negligible coercivity further supports weak ferromagnetic ordering. At 5 K, small coercivity (230 Oe in ZFC, 570 Oe in FC) and vertical *M–H* shifts resemble diluted-antiferromagnetic systems rather than exchange bias effects. Hence, it is noticed that Mg/Zn-substituted ZnO matrices exhibit paramagnetic behavior with weak ferromagnetic interactions at low temperatures, making them suitable for controlled paramagnetic applications rather than room-temperature spintronics. To sum up, the Zn/Mg replacement mechanism can be considered an ideal option to improve the fundamental characteristic features of the ZnCoO matrix for use in real-world technological applications by stabilizing the crystal structure. Further studies, such as electron spin resonance or first-principles calculations, could provide deeper insights into the role of Mg in tuning magnetic interactions in ZnO-based DMS systems.

Data availability

No datasets were generated or analysed during the current study.

Author contributions OO, EA, and TS conceived the idea for the project and designed the experiments. TS, CT, ASE, and EA performed methodology, project administration, investigation, also performed materials production. GY, OO, and CT performed experimental measurement and resources, formal analysis, review & editing. CT, EA, OO, and GY performed writing - original draft, writing - review & editing. All authors discussed the results and commented on the manuscript.

Compliance with ethical standards

Conflict of interest The authors declare no competing interests.

References

1. Dierolf V, Ferguson IT, Zavada JM (2016) Rare earth and transition metal doping of semiconductor materials: Synthesis, magnetic properties and room temperature spintronics. Woodhead Publishing, Cambridge
2. Shiraki Y, Usami N (2011) Silicon-germanium (Sige) nanostructures: production, properties and applications in Electronics. Woodhead Pub, Cambridge, UK
3. Kumar P (2023) Defect induced magnetism in oxide semiconductors. S.l. Woodhead Publishing
4. Ray S (2020) Magnetism and spintronics in carbon and carbon nanostructured materials. Elsevier, Amsterdam, Netherlands

5. Hasan GM, Banna UL, Park K (2020) J Ceram Process Res 21:656–661
6. Tuana DA, Vuong LD, Tung VT, Tuan NN, Duong NT (2018) J Ceram Process Res 19:32–36
7. Zhengwu J, Murakami M, Fukumura T, Matsumoto Y, Ohtomo A, Kawasaki MH (2000) J Cryst Growth 214:55–58
8. Heiba ZK, Arda L, Mohamed MB, Mostafa NY, Dogan N (2013) J Supercond Nov Magn 26:3487–3493
9. Kilic N, Ozturk S, Arda L, Altindal A, Ozturk ZZ (2012) J Alloy Compd 536:138–144
10. Iwan S, Dianisya D, Fahdiran IR, Budi E, Budi SA, Handoko E (2019) J Ceram Process Res 20:518–521
11. Dietl T, Ohno H, Matsukura F, Cubert J, Ferrand D (2000) Science 287:1019–1022
12. Snoek JL (1946) Philips Techn Rev 8:353–360
13. Neel L (1948) Ann Phys Ser 12:137–198
14. Fan Z, Lu JG (2005) J Nanosci Nanotechnol 5:1561–1573
15. Feltham P, Banerjee R (1992) J Mater Sci 27:1626–1632
16. Pearton SJ, Abemathy CR, Overberg ME, Thaler GT, Norton DP, Theodoropoulou N et al. (2003) J Appl Phys 93:1–13
17. Pei G, Xia C, Wu F, Xu J (2009) J Alloy Comp 467:539–542
18. Konana FK, Betied A, Nkuissi HJT, Dakshi K, Aka B, Hartiti B (2017) J Ceram Process Res. 18:882–886
19. Kim KW, Sun KJ, Lee SN (2012) J Ceram Process Res 13:291–294
20. Siddheswarana R, Mangalaraja RV, Ricardo AE, Maria EG, Manikandan D, Lopez M et al. (2012) J Ceram Process Res. 13:801–805
21. Xie Z, Zou Z, Mao Z, Jiang X, Zhang W (2022) Room-temperature structure, magnetic, and magnetocaloric properties of (La0.8-xNdx)Sr0.2MnO3($0 \le x \le 0.2$). J Mater Res. Technol 21:2778–2796
22. Xie Z, Zheng X, He W, Feng M, Xu C, Zou Z (2025) Effects of Cr3+ incorporation on structure, surface morphology, and the magnetocaloric effect in La0.8Sr0.2Mn1-xCrxO3 ceramics by means of first-principles calculations and wet chemical method. Ceram Int 51:10026–10040
23. Xie Z, Zou Z, Xu C, Zhong S, Feng M, Jiang X, Zhang W, Zheng X, He W (2024) Changes in microstructure, magnetocaloric effect and critical behavior of La0.8Sr0.2MnO3 manganites by K/Co doping. Chin J Phys 90:387–409
24. Jlassi M, Sta I, Hajji M, Ezzaouia H (2014) Effect of nickel doping on physical properties of zinc oxide thin films prepared by the spray pyrolysis method. Appl Surf Sci 301:216–224
25. Xie Z, Zou Z, Jiang X, Zhang W (2023) Effects of A, B-site multiple ion co-doping on the structure, magnetic, magnetocaloric effect, and critical behavior of La0.7-xNd0.1Sr0.2KxMn0.95Ni0.05O3 ceramics. Ceram Int 49:32663–32678
26. Xie Z, Zou Z, He W, Zhong S (2024) Influences on the structure, magnetic, and magnetocaloric effect of La0.8Sr0.2MnO3 ceramics by Co ion doping with sol-gel method and first-principles calculations. Ceram Int 50:47926–47938
27. Alrowaili ZA, Abdeltwab E, Atta A, Taher FA (2020) Controlled growth of hexagonal nanocrystals Co and Gd co-doping ZnO by hydrothermal method. Emerg Mater Res. 9(2):1–9
28. Chauhan R, Kumar A, Chaudhary RP, Tripathi SK, Dharamvir K, Kumar R, Saini GSS (2011) Synthesis and optical properties of nickel doped zinc oxide nanoparticles. AIP Conf Proc 1393:319
29. Cullity, B. D., Stock, S. R. (2001) Elements of X-ray diffraction, 3rd ed. Prentice Hall
30. Asikuzun E (2016) Ph D thesis. Abant Izzet Baysal University, Turkey
31. Tian GL, He HB, Shao JD (2005) Effect of microstructure of TiO_2 thin films on optical band gap energy. Chin Phys Lett 22:1787–1789
32. Jiu JT, Wang FM, Adachi M (2004) Preparation of highly photocatalytic active nano-scale TiO_2 by mixed template method. Mater Lett 58(30):3915–3919
33. Al-Ghamdi AA, Al-Hartomy OA, El Okr M, Nawar AM, El-Gazzar S, El-Tantawy F, Yakuphanoglu F (2014) Semiconducting properties of Al doped ZnO thin films. Spectrochim Acta Part A Mol Biomol Spectrosc 131:512–517
34. Jain GH, Patil GE, Mogal GJ, Ahire DV, Patil RL, Kajale DD., Gaikwad VB (2014) Preparation of Ni-doped ZnO nanorods by hydrothermal route for gas sensor applications. In: Mason A, Mukhopadhyay SC, Jayasundera KP, Bhattacharyya N (eds) Sensing technology: current status and future trends I. Springer International Publishing, Chem, pp 195–207
35. Shirage PM, Rana AK, Kumar Y, Sen S, Leonardi SG, Neri G (2016) Sr- and Ni-doping in ZnO nanorods synthesized by a simple wet chemical method as excellent materials for CO and CO_2 gas sensing. RSC Adv 6:82733–82742
36. Shrisha BV, Bhat S, Kushavah D, Gopalakrishna Naik K (2016) Hydrothermal growth and characterization of Al-doped ZnO nanorods. Mater Today Proc 3:1693–1701
37. Elmustafa AA, Stone DS (2003) J Mech Phys Solid 51:357–381
38. Gong J, Wu J, Guan Z (1999) J Eur Ceram Soc 19:2625–2631
39. Tonejc AM, Djerdj I, Tonejc A (2002) Mater Sci Eng C 19:85–89
40. Camerucci MA, Urretavizcaya G, Cavalieri AL (2001) J Eur Ceram Soc 21:1195–1204
41. Michalek M, Sedlacek J, Parchoviansky M, Michalkova M, Galusek D (2014) Ceram Int 40:1289–1295
42. Rice RW, Wu CC, Borchelt F (1994) J Am Ceram Soc 77:2539–2553
43. Kaya S, Akcan D, Ozturk O, Arda L (2018) Ceram Inter 44:10306–10314
44. He LH, Swain MV (2009) J Biomed Mater Res. A 91:352–359
45. El-Safty S, Silikas N, Akhtar R, Watts DC (2012) Dent Mater 28:1171–1182
46. Sinha SK, Briscoe BJ (2009) Polymer tribology. Imperial College Press, London
47. Bradby JE, Kucheyev SO, Williams JS, Leung JW, Swain MV, Munroe P et al. (2002) Appl Phys Lett 80:383–385
48. Wong S, Haberl B, Williams JS, Bradby JE (2015) J Appl Phys 118:1–6
49. Bull SJ (2005) J Phys D Appl Phys 38:393–413
50. Bradby J, Williams J, Swain M (2004) J Mater Res 19:380–386
51. Fischer-Cripps AC (2000) Introduction to contact mechanics. Springer, New York
52. Roy TK (2015) Mater Sci Eng A 640:267–274